Plasmon-enhanced fluorescence (bio)sensors and other bioanalytical technologies

Dario Cattozzo Mor [a,b,1], Gizem Aktug [a,b,1], Katharina Schmidt [c,1], Prasanth Asokan [a], Naoto Asai [c], Chun-Jen Huang [d,e], Jakub Dostalek [a,c,*]

[a] Laboratory of Biophotonics, FZU-Institute of Physics, Czech Academy of Sciences, Prague, 182 21, Czech Republic
[b] Faculty of Mathematics and Physics, Charles University, Prague, 121 16, Czech Republic
[c] Laboratory for Life Sciences and Technology, Danube Private University, 2700, Wiener Neustadt, Austria
[d] Department of Chemical & Materials Engineering, National Central University, Jhong-Li, Taoyuan, 320, Taiwan
[e] R&D Center for Membrane Technology, Chung Yuan Christian University, 200 Chung Pei Rd., Chung-Li City, 32023, Taiwan

A R T I C L E   I N F O

A B S T R A C T

Advances in the plasmon-enhanced fluorescence method and its implementations in optical sensors, biosensors, and other types of bioanalytical technologies are discussed in this paper. In particular, the focus is given to the results that have been achieved over the last ten years concerning the design and preparation of metallic nanostructures tailored for the amplification of weak fluorescence signals and their utilization in the field of ultrasensitive detection and identification of chemical and biological species. Applications and performance characteristics of plasmon-enhanced fluorescence in the areas of analysis of biomarkers for disease diagnostics, cell imaging, environmental monitoring of harmful compounds, and single molecule analysis are critically reviewed.

1. Introduction

Metallic nanostructures with tailored plasmonic properties became irreplaceable building blocks that currently serve in numerous analytical and bioanalytical technologies [1]. The attractive characteristics of metallic nanostructures are related to their ability to resonantly couple light to surface plasmon modes, which is associated with the enhancement of the intensity of electromagnetic field and local density of optical states occurring in the close vicinity to the metal surface. Such optical resonances were initially utilized for probing of biomolecules and their interaction analysis in a method referred to as surface plasmon resonance (SPR) biosensor [2,3], offering the advantage of direct label-free detection. Moreover, metallic nanostructures in the form of colloidal nanoparticles become routinely employed in lateral flow tests [4] and numerous types of simplified colorimetric assays [5]. When deployed on the surface of solid sensor chips, they also frequently act as extremely efficient substrates for sensitive fingerprinting of molecular analytes by the use of surface-enhanced Raman spectroscopy (SERS) [6] or surface-enhanced infrared absorption spectroscopy (SEIRA) [7]. Among

the plethora of these and other modalities, the area of plasmon-enhanced fluorescence (PEF) emerged through the pioneering works in the research groups of Wolfgang Knoll [8] and Joseph Lakowicz [9]. Their PEF works stemmed from the developments of SPR biosensor-based methods supported by advances in biointerfaces for affinity capture of target analyte species from analyzed liquid samples at the sensor surface. In its various forms, PEF has been referred to also as to surface plasmon field–enhanced fluorescence (SPFS), surface plasmon-coupled fluorescence (SPCE), or metal-enhanced fluorescence (MEF) depending on the means of coupling between the confined surface plasmon field and fluorophore emitters. PEF is a method that takes advantage of increasing the fluorophore brightness (by a factor that can often exceed 10^3) in close vicinity of a metallic surface, where the optical field is tightly plasmonically confined. Such an effect can occur if the spectral position of absorption and emission bands of used emitters overlay with the resonant wavelength of surface plasmon modes and it allows for the accurate distinguishing of output optical signal from background. This functionality paved the way for the design of ultrasensitive sensors and biosensors capable of specific detection of minute

* Corresponding author. Laboratory of Biophotonics, FZU-Institute of Physics, Czech Academy of Sciences, Prague, 182 21, Czech Republic
E-mail address: dostalek@fzu.cz (J. Dostalek).
[1] equal contribution.

amounts of chemical and biological species by using fluorophore labels as well as for the imaging of presence of target species at even single molecule level.

In the last decade, PEF – related optical phenomena gained gradually raising attention of scientific community. Advances in PEF implementations in analytical and bioanalytical tools have been addressed by a range of recent excellent reviews focusing individually on the preparation of suitable plasmonic nanostructures [10], mechanisms important to efficiently utilize PEF in sensors and biosensors [11–13] and more recently on concrete applications [14–16]. This review aims to build upon these works and provide an updated multifaceted view into this rapidly progressing field covering aspects important for the design of plasmonic nanostructures and means by which they can be prepared (section 2), followed by key characteristics of PEF with an overview of reported enhancement factors in relation to complexity and type of plasmonic structures adjusted for specific optical readout configuration (section 3). Afterwards, there are discussed biointerfaces that need to be deployed on the surface of plasmonic nanostructures with a particular focus on the effect of fouling and optimizing the distance between the fluorescent emitters and the metallic surface for specific assay formats (section 4). Then, recent applications where PEF sensors and biosensors are making progress are reviewed: for simplified sensitive detection of molecular species serving for diagnosis of diseases in the biomedical field (section 5), cell imaging (section 6) and for potentially on-site analysis of harmful compounds in the field of environmental monitoring (section 7). Finally, emerging implementation of PEF in single molecule detection and interaction analysis are discussed (section 8) as possible future directions where this type of optics and respective materials can be utilized.

2. Metallic nanostructures supporting surface plasmon resonances

Metallic nanostructures can be designed to manipulate with light via coupling to different types of surface plasmon modes depending on the chosen geometry. The following part provides a brief overview of surface plasmon resonance characteristics and discusses common approaches that have been developed for the preparation of metallic nanostructures. Their overview can be also found in several excellent recent review papers [10,17], and below there is provided a set of examples that are particularly relevant to implementations of PEF sensors biosensors. The choice of the suitable nanofabrication method is crucial with respect to the chosen plasmonic architecture that should take into account the optical readout configuration, the characteristics of the fluorescent emitter, as well as the necessity of capping with appropriate biointerface (as discussed further in more detail).

2.1. Classification of surface plasmon modes

Surface plasmons originate from coupled collective oscillations of charge density and associated electromagnetic field occurring at the surfaces of metals. They can be generated in the form of localized surface plasmons (LSPs) at metallic nanoparticles or as propagating surface plasmons (PSPs) traveling along thin metallic films (as illustrated in Fig. 1a and b, respectively). The properties of such optical modes can be manipulated by the design of metallic structure and one can take advantage of the individual nanoscopic metallic elements serving as building blocks [18]. LSPs excited on individual metallic nanoparticles with a diameter D much smaller than wavelength λ exhibit dipole mode character and the oscillation moment of charge density is parallel to the vector of the driving electric field with intensity $|E_0|^2$. Positioning this nanoparticle at close proximity to a flat surface of a metallic film yields a geometry sketched in Fig. 1c. LSP mode with a tightly confined electromagnetic field and dipole orientation perpendicular to the surface can be excited inside the formed narrow gap spanning over a distance d of several nanometers [19]. A similar gap LSP mode can be generated for the geometry where two metallic nanoparticles are assembled in a dimer configuration (depicted in Fig. 1d) when the distance d between their surfaces is much shorter than nanoparticle size D and wavelength λ [20].

Another coupling regime between LSPs occurs for longer distances between the metallic nanostructure building blocks when they are arranged in periodic arrays (see Fig. 1e). For such geometry with a period comparable to wavelength, diffraction-based interaction can lead to the occurrence of lattice LSP modes [21] with decreased radiative losses and thus increased field intensity enhancement factor $|E/E_0|^2$ [22]. An increasingly rich spectrum of interacting LSP and PSP modes can be orchestrated on geometries of higher complexity that are constituted of different types of metallic nanostructures. Fig. 1f shows an example of a commonly used architecture consisting of a thin metallic film that is perforated with arrays of nanoscopic holes (nanohole arrays) and contacted with periodic arrays of metallic nanoparticles at a defined distance d. This structure supports multiple localized LSP and propagating PSP surface plasmon modes that confine the field intensity in the pores, at walls of metallic nanoparticles, in the gap, or at the inner and outer side of metallic film (see Fig. 1f) [23].
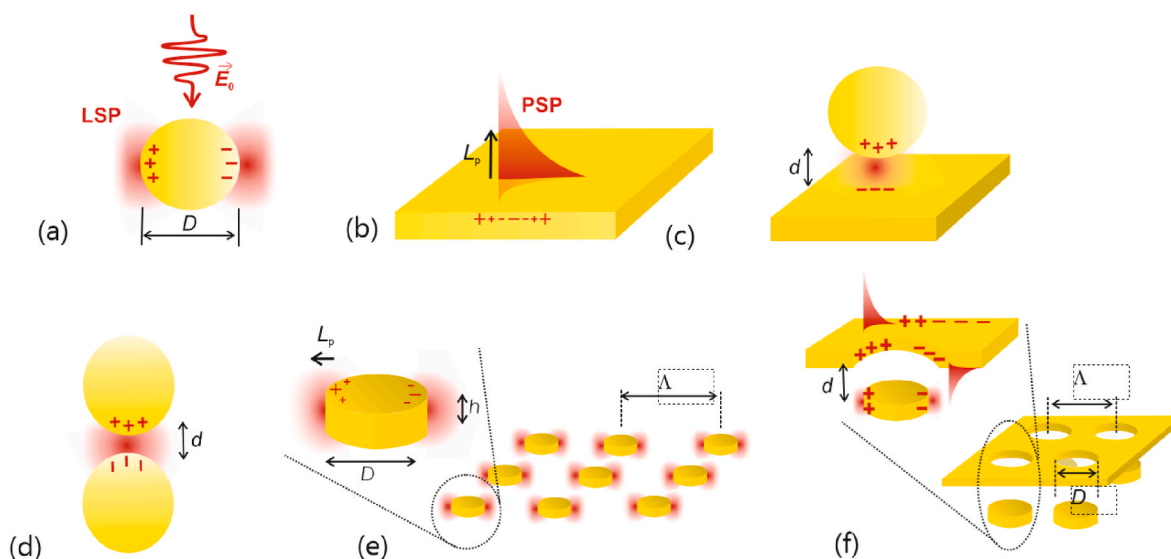

Fig. 1. Examples of geometries that support LSP and PSP modes and their possible coupling.

Optical excitation of surface plasmons is accompanied by spatial confinement of electromagnetic field and respective enhancement of its intensity $|E/E_0|^2$ and local density of optical states (LDOS) [24]. On flat thin metal films, the electromagnetic field intensity of resonantly excited PSPs exponentially decays from the metal interface and typically probes a distance L_p around hundred nanometers. The PSP optical excitation typically provides peak field intensity enhancement $|E/E_0|^2 < 10^2$ (see example in Fig. 2a simulated for PSPs in the red part of the spectrum on Au surface contacted with water). The excitation of LSPs can lead to stronger field intensity enhancement $|E/E_0|^2 > 10^2$ due to the tighter field confinement and respective shorter probing distances L_p from several nanometers to tens of nanometers. An example in Fig. 2b shown for Au disk nanoparticles contacted in water demonstrates that the LSP field intensity enhancement can be increased by diffraction coupling. This effect occurs on periodic arrays of metallic nanoparticles accompanied with the occurrence of lattice LSP modes when the refractive index of the medium below and above the structure is similar. The locations on metallic nanostructure, where particularly strong surface plasmon-enhanced electromagnetic field intensity occurs, are often referred as to plasmonic hotspots. For very narrow gaps $d < 10$ nm in e.g. metallic nanoparticle dimers, the coupling of LSPs via their near field can provide enhancement of field intensity reaching a factor $> 10^3$ at such hotspot positions, see Fig. 2c.

2.2. Preparation of plasmonic nanostructures

Among the 'top-down' approaches, high-precision tools such as electron beam lithography (EBL) or focused ion beam milling (FIB) are frequently employed for the preparation of complex structures with (almost) ultimate control on shape. For instance, they have been used for fabricating of PEF 'antenna-in-a-box' structure composed of a metallic nanoparticle dimer [26] or zero-mode waveguide in a 'horn antenna' format [27]. However, the use of such approaches is typically restricted to research studies and is not suitable for routine bioanalytical applications due to the limited fabrication throughput (dictated by the small area that can be structured) and the high operating costs required for these lithographical techniques. For more practical sensing applications, an important aspect is the possibility of scaling up the preparation of metallic nanostructure for their implementation into e.g. disposable sensor chips. Fig. 3a shows an example of periodic arrays of metallic nanoparticles prepared by UV-laser interference lithography that was shown to be capable of fabrication structures with tuneable plasmonic properties over a large cm^2 area [28]. In this method, a thin photoresist layer is exposed to a UV light interference pattern, followed by the development step and transfer to a thin metallic film with the use of dry etching [28] or lift-off process [29]. Another frequently chosen method for high throughput preparation of well-controlled metallic nanostructures is UV nanoimprint lithography (UV-NIL). It relies on stamps that allow for repeated transfer of desired nanostructure motifs to a UV-light curable resin. As indicated in Fig. 3b, the imprinted topography can be coated with metal films to yield plasmonic diffraction gratings [30], nanohole arrays [31,32], coupled metallic nanoparticle and nanohole arrays [23], and metallic nanoparticle arrays can be prepared by UV-NIL combined with lift-off process [33].

An alternative to 'top-down' approaches is represented by a set of methods that are referred to as 'bottom-up'. Chemically synthesized colloidal nanoparticles can be capped with chemical moieties enabling their trapping at the interface between immiscible phases, leading to the formation of organized lattices due to interfacial electrostatic interactions, capillarity, and van der Waals forces. The Langmuir–Blodgett (LB) method, a classical representation of this technique, utilizes a liquid–air interface for self-assembly into ordered monolayers. These monolayers are then compressed using an LB trough and transferred onto solid substrates, fabricating densely packed, extended 2D structures [34,35]. In another approach, pre-prepared colloidal plasmonic nanoparticles are dispersed in a solvent that is let to evaporate on the
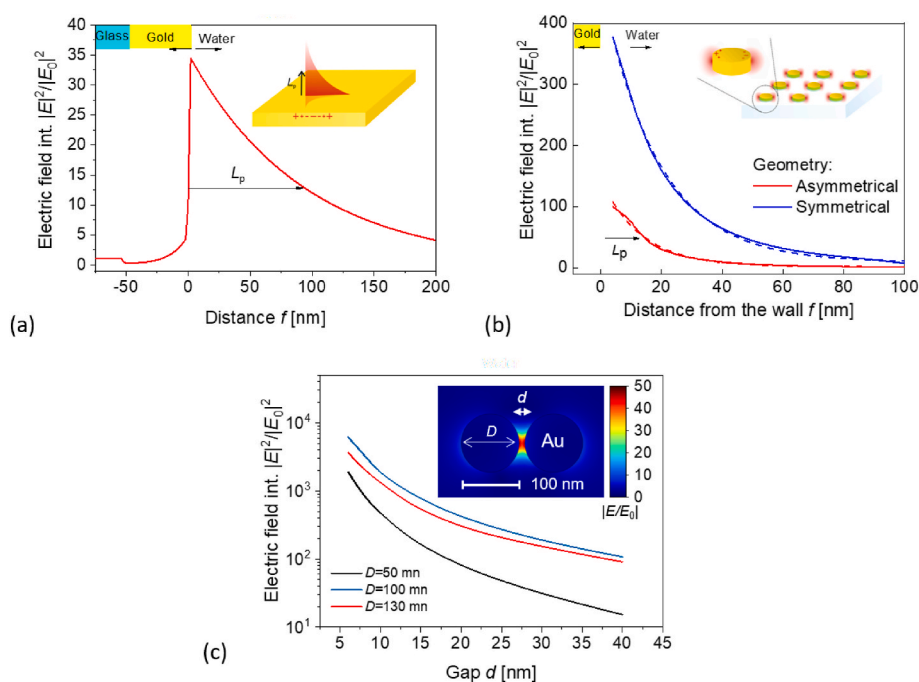

Fig. 2. Profile of a surface plasmon field of a) resonantly excited PSPs by Kretschmann configuration on a 50 nm thick gold film in contact with water (refractive index of 1.33) at a wavelength of 633 nm (obtained by simulations based on transfer-matrix formalism of Fresnel reflectivity) and b) LSPs on arrays of cylindrical nanoparticles with a diameter of $D = 140$ nm and height $h = 50$ nm in the refractive index asymmetrical (refractive index of substrate and superstrate of 1.45 and 133, respectively) and nearly symmetrical geometry (refractive index of substrate and superstrate of 1.34 and 1.33, respectively) obtained by finite difference time domain method and adapted from Ref. [25] with permission from WILEY VCH Verlag GmbH & Co. KGaA, Weinheim. c) LSPs supported by spherical Au nanoparticle dimer embedded in dielectric with refractive index $n = 1.33$ and diameter D and gap d stated in the graph simulated by finite element method with details provided in supporting information.
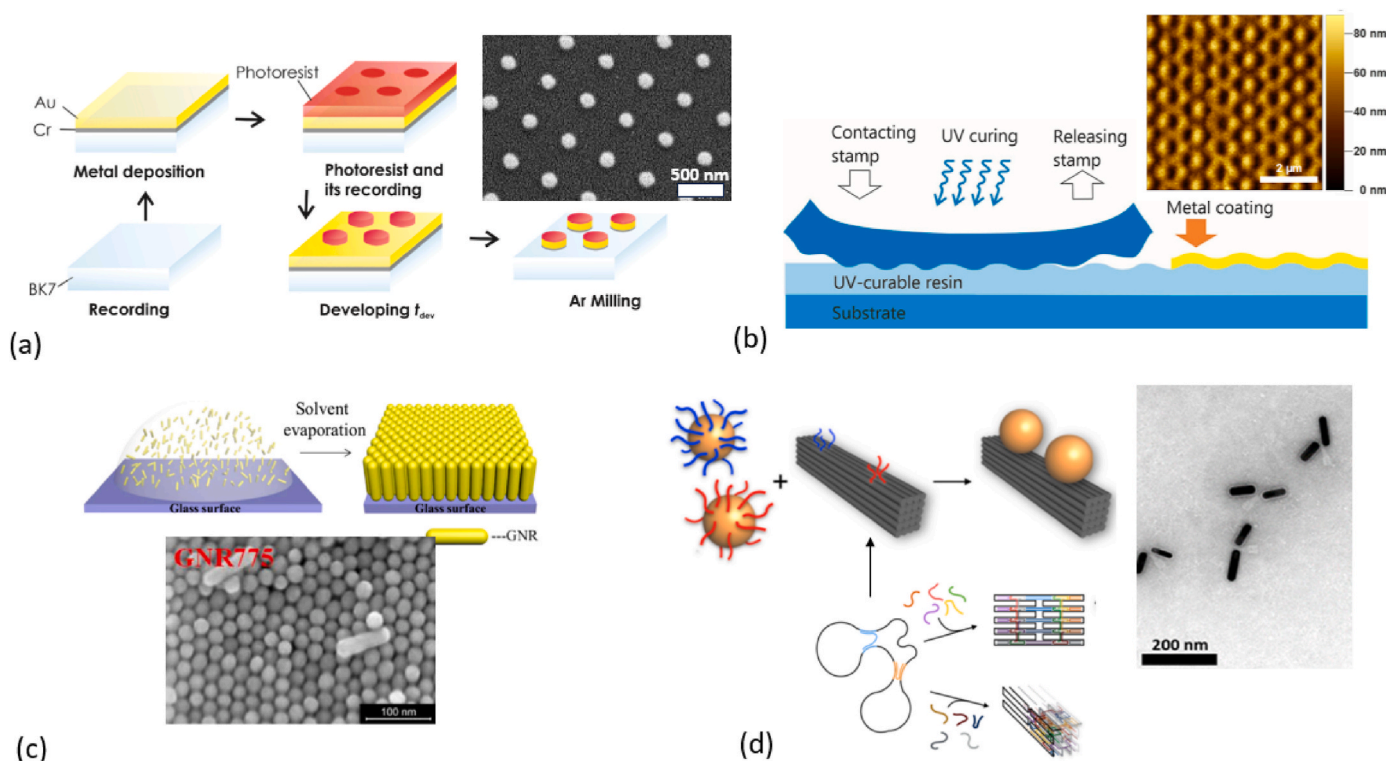
Fig. 3. Examples of the techniques used for the preparation of metallic nanostructures based on a) UV laser interference lithography (reproduced from Ref. [28] with permission from the Royal Society of Chemistry), b) UV nanoimprint lithography (adapted from Ref. [30] with permission from de Gruyter, Berlin/Boston), c) self-assembly of colloidal metallic nanostructures (reproduced from Ref. [36] with permission from American Chemical Society), and d) by selective docking of colloidal metallic nanostructures to DNA origami scaffolds (adapted from Refs. [37,39] with permission from American Chemical Society).

substrate under controlled temperature and humidity conditions. During solvent evaporation, capillary forces draw the nanoparticles closer together, facilitating their self-assembly that has been utilized for the fabrication of highly ordered 2D [36] or 3D [35] plasmonic nanostructures (see Fig. 3c). In the realm of self-assembly-based nanofabrication techniques, DNA nanotechnology rapidly gains momentum and frequently serves for the preparation of precisely controlled metallic nanoparticle structures [37]. In these materials, a long single-stranded DNA scaffold is folded by hybridizing it with a pool of short single-stranded DNA (ssDNA) oligonucleotides acting as staples. Specific staple strands can be modified with molecules of interest or serve for accurate docking of colloidal metallic nanoparticles carrying complementary short ssDNA strands (see Fig. 3d). This strategy allowed for the preparation of a wide range of assemblies from metallic nanoparticles including planet-satellite structures [38], controllable dimer nanoparticle plasmonic nanoantennas [39], or even more complex spiral assemblies [40] and structures that can be actively reconfigured by affinity interaction with ssDNA molecules with a toehold [41].

3. Surface plasmon-enhanced fluorescence

The coupling of fluorophore emitters with metallic nanostructure is commonly described by using a model introduced below that is applicable for the majority of conditions used in PEF sensors and biosensors. The maximizing of PEF efficiency requires orchestrating a range of parameters which were identified by former fundamental studies on the interaction of individual fluorescence emitters with metallic nanomaterials [42,43]. These investigations revealed that balancing the enhancement and quenching of fluorescence is crucial. Certain geometries of plasmonic structures, particularly with narrow gaps, were already more than a decade ago demonstrated to reach *EF* values above 10^3 [44,45] and more recent progress is discussed further.

3.1. Coupling between fluorescent emitters and surface plasmons

As schematically shown in Fig. 4a, the coupling of fluorescent emitters with the confined electromagnetic field of surface plasmons alters their emission characteristics and it is often described by the excitation rate γ_e, radiative emission rate γ_r and non-radiative decay rate γ_{nr}. In general, these rates refer to transitions that can be mediated by surface plasmons at both absorption wavelength λ_{ab} (γ_e) and emission wavelength λ_{em} (γ_r) of an emitter that can take the form of organic dye molecules, quantum dots (QD) [46], or upconverting nanocrystals [47]. For fluorescent emitters with short Stokes shift comparable with a spectral width of SPR band (e.g. most common organic dye emitters), the metallic nanostructure supporting surface plasmons can be simultaneously coupled at both λ_{ab} and λ_{em}. The emitters with wide spectral separation of absorption and emission bands may be engineered to couple with surface plasmons only via one of these channels. Let us note that emitters with lifetime in ns time range (emitting fluorescence signal) are dominantly utilized in PEF sensors and biosensors and therefore configurations with emitters exhibiting longer μs – ms lifetime such as rare earth chelates [48] are not discussed further. Moreover, the coupling of emitters with the metallic nanostructure is operated far from the conditions explored for the strong coupling regime [49] and that the excitation rate is far from saturation ($\gamma_e \ll \gamma_r$) in common fluorescence spectroscopy-based biosensors and assay readout conditions. Then, the radiative emission rate γ_r at λ_{em} that is proportional to the measured fluorescence signal can be described by using a semiclassical picture [24] as the following product:

$$\gamma_r \sim \left| \vec{E}(\lambda_{ab}) \cdot \vec{\mu}_{ab} \right|^2 \times \eta \times CE\left(\vec{\mu}_{em}, \lambda_{ab} \right) \tag{1}$$

where $\vec{E}$ is the electric intensity vector of the excitation light beam at λ_{ab}, $\vec{\mu}_{ab}$ is the absorption dipole of the fluorescent emitter, η is the
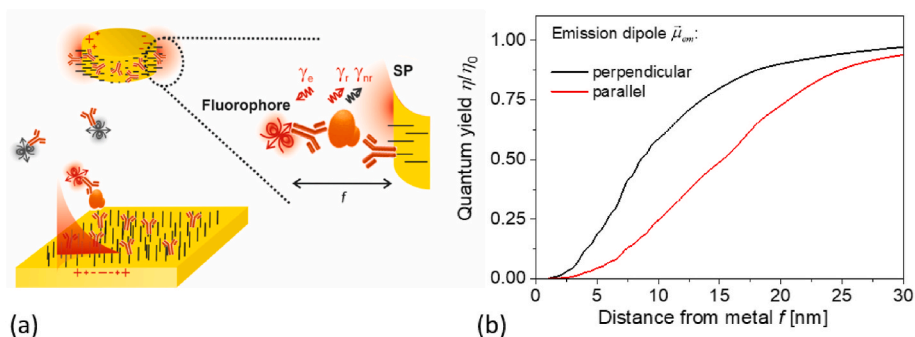
Fig. 4. a) Schematics of the coupling of fluorescent emitters with confined electromagnetic field of surface plasmons at the emitter when employed in sandwich immunoassay and b) distance-dependent changes in quantum yield in the red part of the spectrum for flat Au surface (adapted from Ref. [51] with permission from American Chemical Society).

emitter quantum yield, and CE states the collection efficiency of emitted photons at λ_{em} of the used optical system. The first term corresponds to the excitation rate γ_e, which can be locally increased by the plasmonic enhancement of the field intensity $|E/E_0|^2$ at λ_{ab}. Importantly, this interaction depends on the orientation of the emitter taken into account by the $\overrightarrow{\mu}_{ab}$ vector and there may be considered whether it is static (e.g. emitters embedded in dense polymer films [50]) or allowed to freely rotate (when e.g. immobilized via flexible polymer chains to the surface [51]).

The second term defines the dependence of the emitter quantum yield $\eta = \gamma_r/(\gamma_r + \gamma_{nr})$ that is either increased by the surface plasmon-enhanced LDOS (affecting γ_r, particularly for emitters with low inherent quantum yield η_0 [52,53]) or decreased through the effect of quenching γ_{nr}. The quenching occurs in very close proximity to metals and it is strongly dependent on the distance f of the emitter from the surface. As illustrated by simulations in Fig. 4b, this effect is pronounced at distances f below about 15 nm and it is stronger for emission dipole

$\overrightarrow{\mu}_{em}$ orientation parallel to the surface compared to the perpendicular one. The effect of distance-dependent fluorescence emission intensity was experimentally investigated at single molecule level on flat Au film [54] and for Au nanoparticle [42]. These studies revealed that the optimum distance for PEF that balances the plasmonic enhancement and effect of quenching is shorter for metallic nanoparticles supporting LSPs ($f = 5$ nm for Nile Blue interacting with 80 nm diameter Au spherical NP [42]) than that on continuous metallic films along which PSPs propagates ($f = 30$ nm for DiIC1(5) attached to Au surface).

The third term CE states for the collection efficiency that can be particularly improved for plasmonic systems, where the emission to the far field occurs via surface plasmons. Directional emission on e.g. tailored diffraction gratings [55–57] or plasmonic particle assemblies acting as nanoantennas [58–60] offers means for improved extraction of emitted fluorescence light in optical systems that image the fluorescent object to a detector by using optics with lower numerical aperture.
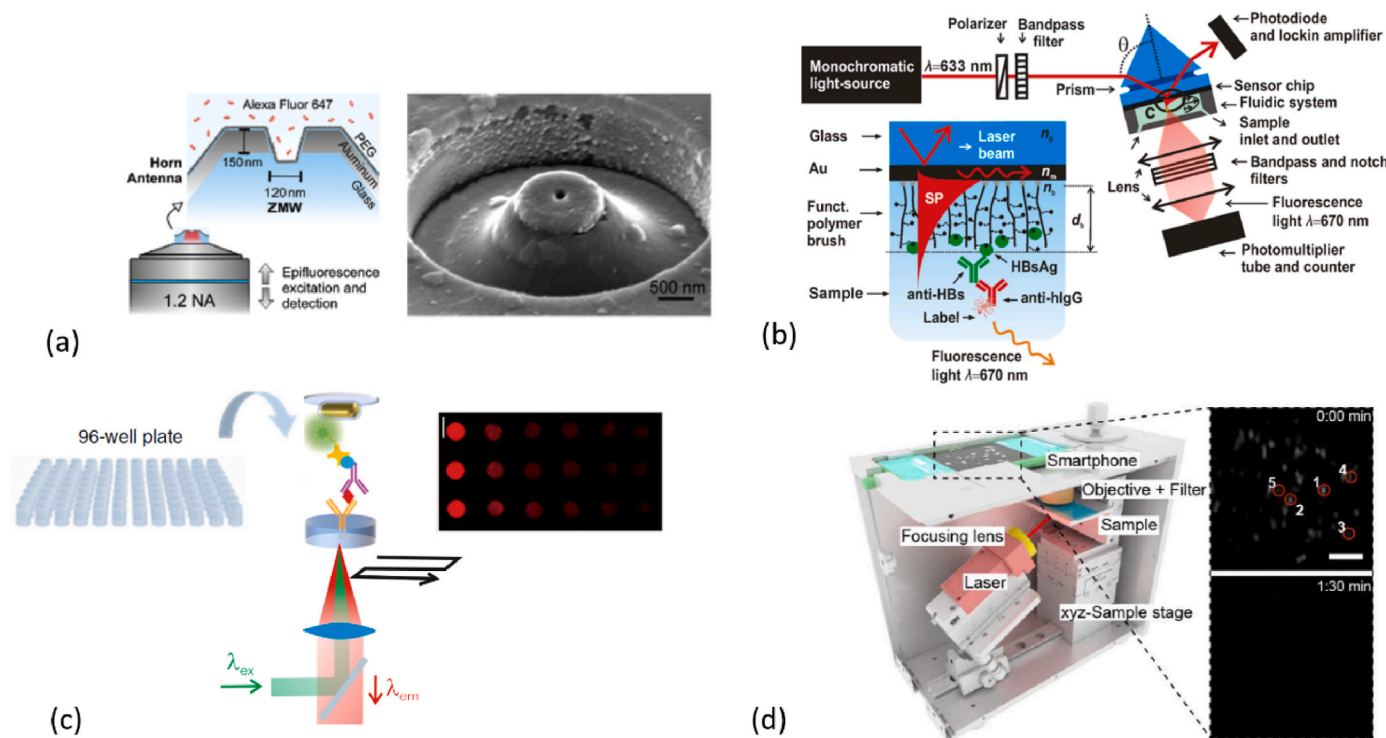
Fig. 5. Optical system for PEF utilizing a) confocal microscopy with a structure designed to excite LSPs at a nanopore (adapted from Ref. [27] with permission from Wiley-VCH GmbH), b) probing by PSP modes with attenuated total reflection method and Kretschman geometry (adapted from Ref. [65] with permission from American Chemical Society), c) scanning epi-illumination microscopy (adapted with permission from Ref. [66]) and d) wide-field microscopy using a smartphone-embedded detector (reproduced with permission from Ref. [68]).

3.2. Optical readout systems

The most commonly used optical systems for PEF-based assay readout rely on established optical configurations for wide-field fluorescence microscopy and confocal laser scanning microscopy (CLSM). In most cases, the excitation and collection of emitted radiation is performed by the same objective lens using the epi-illumination configuration (see Fig. 5a). In wide-field fluorescence microscopy, selected area on the sensor chip is illuminated by an excitation beam with wavelength λ_{ex} (that is close to the emitter absorption wavelength λ_{ab}) and the emitted fluorescence light at wavelength λ_{em} is imaged to a CCD or CMOS-based camera. CLSM approach relies on scanning the excitation beam at λ_{ex} over the surface and fluorescence light at λ_{em} is detected by a photomultiplier or avalanche photodiode. This setup allows for efficient suppressing of background by blocking of light emitted from outside the focal volume of objective lens, but typically provides a slower readout. Both wide-field and CLSM configurations are largely used in the context of microarray scanners deployed in standard molecular biology laboratories [61] (see Fig. 5b). CLSM is often used with high numerical aperture objectives for high spatial resolution measurements that require optical matching to the analyzed substrate to the objective. The wide-field imaging can be utilized for examining larger areas with weaker magnifying optics featuring lower numerical aperture imaging systems that can e.g. benefit from directional surface plasmon-coupled emission [see term CE in equation (1)].

In addition, total internal reflection fluorescence microscopy (TIRF) is often utilized in order to excite emitters via evanescent wave generated at λ_{ex} generated upon total internal reflection at the sensor surface [62]. Its intensity exponentially decays away from the interface, reaching distances comparable to the used wavelength. This configuration has been utilized for Kretschmann configuration-based excitation of PSPs on thin metal films in a method referred to as surface plasmon-enhanced fluorescence spectroscopy – SPFS [8]. This method allows for probing short distances f of about 100 nm from the metallic surface and it was implemented in combination with other bioanalytical tools such as SPR biosensors [63], see Fig. 5c. For the investigation of more complex biointerfaces and probing larger analytes, the utilizing of optical waveguide spectroscopy was reported with the use of the same optical platform and enhanced evanescent field intensity penetrating to deeper up to micrometer distances [64].

Advances in the smartphone-based technologies enabled using these devices as detector output units in numerous fluorescence-based analytical systems, which is particularly useful in point-of-need settings for the detection of cells, bacteria, viruses, and biomarkers. These mobile microscopy devices are pursued to provide cost-effective, field-portable, and easy-to-use alternatives to established benchtop devices deployed in laboratories. Recent developments in smartphone camera technology have improved their performance, approaching that of scientific-grade detectors as demonstrated by fluorescence microscopy of DNA origami constructs with predefined numbers of fluorophores to quantify the sensitivity. The sensor exhibited a detection limit of ~10 fluorescent dyes per diffraction-limited spot [67]. These types of detectors were tested with a simplified microscopy optical systems showing that in conjunction with PEF (providing an average EF of 89 ± 7) single fluorescent emitters are detectable [68]. Other examples include dual-wavelength fluorescence biosensors equipped with smartphone imaging [69].

3.3. Comparison of PEF structures and geometries

Fluorescence enhancement factor EF is a key characteristic used for the comparison of PEF performance and it can be defined as a ratio of the emitted photon flux delivered to a detector from a fluorophore attached to the amplifying plasmonic structure γ_r compared to that from the same emitter without the structure γ_{r0}:

$$EF = \gamma_r / \gamma_{r0}. \tag{2}$$

In general, it is not a universal characteristic of the metallic nanostructure but, as equation (1) indicates, it depends on the properties of the emitter (e.g. its quantum yield in the bulk medium η_0) as well as on the optical configuration (affecting the collection efficiency CE), and the ability to position the emitters at locations probed by the surface plasmon field (plasmonic hotspots where the field intensity enhancement $|E/E_0|^2$ and LDOS peak). To account for the strong dependence of the fluorescence enhancement on the intrinsic fluorophore's quantum yield η_0, an alternative way to quantify PEF performance was proposed [39] by using the figure of merit defined as:

$$FoM = EF \cdot \eta_0. \tag{3}$$

This section provides an overview of implementations of PEF illustrating the relation between EF and the metallic nanostructure geometry, the preparation route, and readout configuration. It aims at providing a guide to the reader towards the most suitable options for their intended use and Table 1 presents a set of relevant examples of recent works.

One of the highest EF values was obtained in narrow gaps between metallic nanostructures. It can be utilized as metallic nanoparticle dimer (see Fig. 1d) with fluorophores placed in the formed nanoscale gap of $d = 5$–10 nm. Such geometry supports tightly confined LSP field intensity that is enhanced by a factor rapidly increasing when closing the gap distance d (see Fig. 2c). In one route, such geometry was lithographically prepared by EBL in combination with template stripping in order to yield flat arrays of plasmonic nanoantennas [26]. They were constructed from Au half-spheres with 10 nm nanogap and a diameter of $D = 80$ nm that were optimized for single-molecule analysis in a detection volume of about 20 zL. This approach was reported to reach $EF = 5.3 \times 10^3$ for Alexa Fluor 647 fluorophores with decreased quantum yield η by quenching. In order to simplify the preparation route, aggregation of colloidal gold nanoparticles into dimers or trimers was reported by using drop-casting for PEF studies [70]. The tuning of the gap was facilitated by capping the chemically synthesized nanoparticles with a sacrificial polyethylene glycol spacer. For a gap size close to 6 nm there was achieved EF of 600 for the same quenched Alexa Fluor 647 fluorophore. A similar structure with end-to-end orientation of synthesized Au nanorod particles featuring a separation gap of 5 nm was used for the two-photon excitation of Atto 610 emitters diffusing in a liquid solution [71]. Owing to quadratic dependence on the excitation field intensity $|E/E_0|^4$, an extraordinarily high enhancement factor EF of 5×10^7 was reported for molecules passing through the plasmonic hotspot compared to that in the bulk solution. In a similar experiment with individual Au nanorod particles and quantum dot emitter, a lower enhancement factor of $EF > 10^4$ was reached [72] which can be ascribed to weaker excitation field strength.

In another route, precise controlling of nanogaps between plasmonic nanoparticle dimers where fluorophores can be positioned has been explored by using DNA origami constructs [73]. In this approach, three-dimensional DNA origami scaffolds were self-assembled in the form of a pillar carrying specific docking sites for two chemically synthesized metallic nanoparticles, with a cleared hotspot in between for the incorporation of a fluorophore (see Fig. 3d). For instance, by using Au nanorods with dimensions 67 nm by 20 nm anchored to the DNA pillar forming a 12 nm dimer gap, there was a reported enhancement factor of $EF = 1.6 \times 10^3$ for Cy7 fluorophores, $EF = 1.4 \times 10^3$ for Atto 740, and $EF = 1.1 \times 10^3$ for Alexa Fluor 750 [74]. The obtained antennas presented a narrow dispersion in dimer gap dimensions (average 11.7 ± 2.7 nm), showing the reproducibility of the proposed self-assembly technique and assuring strong field enhancement at the fluorophore location. On the other hand, when compared to the lithographic fabrication technique of the previous example, this work reported a larger deviation in the antenna geometry (angle between the longitudinal axes

Table 1

Examples of metallic nanostructures designed for plasmon-enhanced fluorescence illustrating the relation between enhancement factor *EF* and *FoM*, employed fabrication technique for metallic nanoparticle (NP) preparation, optical readout configuration, and used fluorophore. *FoM* states values reported or deduced from *EF* and quantum yield of emitters η_0 when available.

Plasmonic structure	*EF/FoM*	Fabrication technique	Readout geometry	Fluorophore	Ref.
Colloidal metallic NPs assembled *via* DNA origami					
Au nanorod NP dimer	$1.1–1.7 \times 10^3$/483	DNA origami, gap of 12 nm	Inverted confocal fluorescence microscope	Cy7, Atto 740, Alexa Fluor 750	[74]
Au spherical NP dimer	5.5×10^3/306	DNA origami, gap of 12–17 nm	Inverted confocal fluorescence microscope	Atto 647 N	[39]
Ag spherical NP dimer	4.5×10^2/152	DNA origami, gap of 12 nm	Wide-field fluorescence microscope with smartphone detector	Alexa Fluor 647	[68]
Colloidal metallic NP and their other assemblies					
Ag nanocubes NP on Au surface	1.5×10^2	Chemical synthesis of NP	Confocal fluorescence microarray scanner	Alexa Fluor 647	[61]
Au spherical NP dimers	5.8×10^2/46	Aggregation of chemically synthesized NPs	Inverted confocal fluorescence microscope	Alexa Fluor 647 with quencher	[70]
Sub-diffractive Au NP arrays	$4.5–70 \times 10^3$/ $1.2–19 \times 10^3$	Self-assembly, block copolymer micelle nanolithography	Wide-field inverted fluorescence microscope	Cy5	[76, 77]
Au nanorod NP	$>10^4$	Chemical synthesis of NP	Confocal fluorescence microscope	Qdot 655 (two-photon excitation)	[72]
Au nanorod NP dimer	5×10^7	End-to-end assembly with sacrificial molecular linker	Confocal fluorescence microscope	Atto 610 (two-photon excitation)	[71]
Metallic nanostructures prepared by lithography					
Au multi-period plasmonic grating	3.0×10^2/12	UV-LIL/UV-NIL	Wide-field epi-illumination microscope	Alexa Fluor 790	[30]
Au nanohole/disk Arrays	1.0×10^2/30	EBL/UV-NIL	Attenuated total internal reflection	Alexa Fluor 647	[56]
Au antenna in a box	5.3×10^3/420	EBL	Inverted confocal fluorescence microscope	Alexa Fluor 647 with quencher	[26]
Au nanohole/disk arrays	$3.0–4.1 \times 10^2$/12 - 17	Nanosphere lithography with Ar milling	Fluorescence spectrometer with right-angle configuration	Alexa Fluor 790	[78]

of the Au nanorods of $134 \pm 33.8°$) leading to increased variation in the LSPR wavelength (varying between 650 and 910 nm) and respective changes in *EF*. Similar DNA origami geometry was proposed in earlier works, but with the use of gold nanospheres instead of nanorods [39,75] providing lower fluorescence *EF* of about 0.5×10^3 given by weaker field confinement. Both classes of PEF structures were used for confocal microscopy – based studies to probe individual antennas.

Colloidal metallic nanoparticles also served as building blocks in other geometries explored for PEF substrates with the possibility of structuring larger surface areas. Block copolymer micelle nanolithography was developed for the self-assembly of closely packed hexagonal periodic arrays of spherical Au nanoparticles. This technique allowed to yield a sub-diffractive lattice of Au nanoparticles with a diameter *D* of 50 nm arranged with a narrow gap *d* of about 20 nm. For PEF substrates prepared by such a potentially scalable fabrication method, an extraordinarily high fluorescence enhancement factor of *EF* $> 10^4$ was reported for Cy5 emitter [76] with a wide-field fluorescence microscope. The same research group expanded the earlier work by making the plasmonic substrate dual-resonant for coupling the LSPR wavelength with the emission/excitation peaks of Cy5 and 5-Carboxyfluorescein (5-FAM), while preserving high enhancement factors reaching *EF* = 4.5×10^3 and 1.6×10^2 for Cy5 and 5-FAM, respectively [77].

In another approach to gap structures, *EF* = 1.5×10^2 was obtained by a sandwich immunoassay with colloidally-synthesized silver nanocubes [61]. The Ag nanocubes were conjugated with an antibody and allow for fluorescence enhancement in the cavity when, in the presence of the antigen, a 20-nm gap is created between the Ag nanostructure and flat gold surface bearing another antibody recognizing the antigen.

In addition to nanostructures supporting the tightly confined electromagnetic field of LSPs, metallic thin films with PSPs traveling along their interface allow for enhancing the fluorescence signal intensity of attached emitters. For flat Au thin films, PEF can be combined with SPR sensors in Kretschmann configuration for resonant excitation of PSPs, providing enhancement factors *EF* $< 10^2$ [79]. The structuring of such thin metallic films offers a route for increasing the enhancement factor *EF* to about 10^2 by e.g. perforating with arrays of nanoholes (see geometry in Fig. 1f) when prepared by the use of UV-NIL [56]. Periodically

corrugated thin metallic films can be designed for diffraction-based coupling to PSPs and such multi-periodic plasmonic gratings prepared by either UV-LIL/UV-NIL [30] or nanosphere lithography [78] were explored for PEF. A structure featuring overlaying periodicities (see Fig. 3b) was designed for simultaneous excitation of PSP modes at two spectral bands overlapping with the fluorophore (Alexa Fluor 790) absorption and emission spectra. By combining the enhancement of the excitation rate and directional surface plasmon-coupled emission, the structure allowed reaching *EF* = 3×10^2, with the use of wide-field fluorescence microscopy in epi-illumination configuration.

4. Biointerfaces and assay formats

Dedicated biointerfaces have been devised for surfaces of metallic nanostructures tailored for optical probing of target analyte molecules with the confined electromagnetic field of surface plasmons. These surface architectures are designed a) to provide controlled docking of biorecognition elements (BREs) that facilitate a specific capture of target species from analyzed liquid samples at the sensor surface and b) to prevent blocking of the sensor surface due to the adsorption of other abundant molecules present in the analyzed sample. The anchoring of BREs is typically realized by the incorporation of chemical handles to the biointerface enabling their conjugation via amine [80] or thiol groups [81] or by using tags bearing moieties such as biotin or azide [82]. The ability to repel fouling was pursued by using a vast range of architectures and the development of such biointerfaces has been subject to numerous recent reviews [83]. This section is dedicated to several key aspects that are of high importance to PEF bioanalytical technologies including a) approaches for selective functionalization of the surface of metallic nanostructures at areas, where the electromagnetic field intensity is confined, and b) at systems that allow for combining antifouling properties with controlling distance of captured molecules from the metal surface.

4.1. Selective functionalization of plasmonic hotspots

In order to fully harness the potential of PEF, the respective structure needs to assure that the optical probing of the target analyte takes place

at the location, where the electromagnetic field is confined by the resonant coupling to surface plasmons. As discussed in the previous section 3.1, this occurs at spatially confined volume in the vicinity to metallic nanostructures referred to as plasmonic hotspots. The following part provides an overview of techniques that were recently explored for the precise attachment of biomolecular species at metallic nanostructures and that can be employed for docking of BREs with nanoscale accuracy.

UV laser interference lithography was employed for the preparation of periodic arrays of nanoscopic spots on solid substrates that are functionalized with hydrogel binding matrix at locations aligned with arrays of Au nanoparticles [84]. This approach relied on photo-activated attachment and crosslinking of poly(N-isopropylacrylamide)-based polymer (pNIPAAm) with benzophenone and carboxylic groups to form a polymer network for subsequent postmodification with immunoglobulin G (IgG) molecules. The yielded responsive biofunctional hydrogel selectively wrapped over the metallic nanostructure in zones where plasmonic hotspot occurs, see Fig. 6a. Similar pNIPAAm-based material was combined with a substrate carrying quasiperiodically arranged plasmonic nanopores in order to serve as actively controllable gates [85]. These responsive polymer gates were demonstrated to allow for on-demand trapping and release of biomolecules in the nanopores that were probed with the confined field of LSP supported by this nanostructure, Fig. 6b.

The orthogonal linker chemistry approach was implemented for the selective coupling of protein molecules at a gap between lithographically made metallic nanoparticles forming a plasmonic hotspot [86]. Arrays of Au nanorod dimers were prepared by EBL on a SiO$_2$ substrate with a TiO$_2$ material deposited in the gap. Then, passivating the Au surface by polyethylene glycol (PEG) molecules with thiol groups was followed by the selective reaction of dopamine-biotin molecule at the TiO$_2$ pad and by filling the SiO$_2$ surface with poly-lysine–PEG. The

yielded structure was then proposed for selective binding of streptavidin at the plasmonic hotspot that overlaps with TiO$_2$ pads.

Plasmon-enhanced photochemistry represents another route that was explored for selective functionalization of metallic nanostructure at plasmonic hotspots. Au nanoparticle assemblies were utilized for plasmonically-assisted ejection of hot electrons at the hotspot location where they selectively desorb thiol self-assembled monolayer (SAM) from the nanostructure [87]. As illustrated in Fig. 6c, such deprotected area can be afterwards backfilled with functional thiol molecules including ssDNA-thiol or thiol-biotin for selective coupling of ssDNA with a fluorophore reporter or streptavidin. In a similar direction, the plasmonically generated hot electrons were employed for local triggering of polymerization at the plasmonic hotspots as seen in Fig. 6d [88]. In conjunction with synthesizing polymers bearing functional units, this approach holds potential for efficient means enabling selective docking of BREs at the plasmonic hotspot.

Chemically synthesized Au nanorod particles exhibit (due to their crystalline structure) anisotropic reactivity that can be exploited for site-specific functionalization at their tips [89]. This property was exploited for the assembly of plasmonic dimer structures based on sacrificial molecular linkers [89]. An increasingly popular approach for the preparation of more complex plasmonic nanostructures from chemically synthesized metallic nanostructures is based on DNA origami [90]. This technology has been implemented for the self-assembly of plasmonic nanoantennas with ssDNA staples that can be engineered to carry additional functional units at the desired location, where the plasmonic hotspot occurs. As Fig. 6e illustrates, these units can be prepared in the form of ssDNA for specific binding of complementary ssDNA strands.
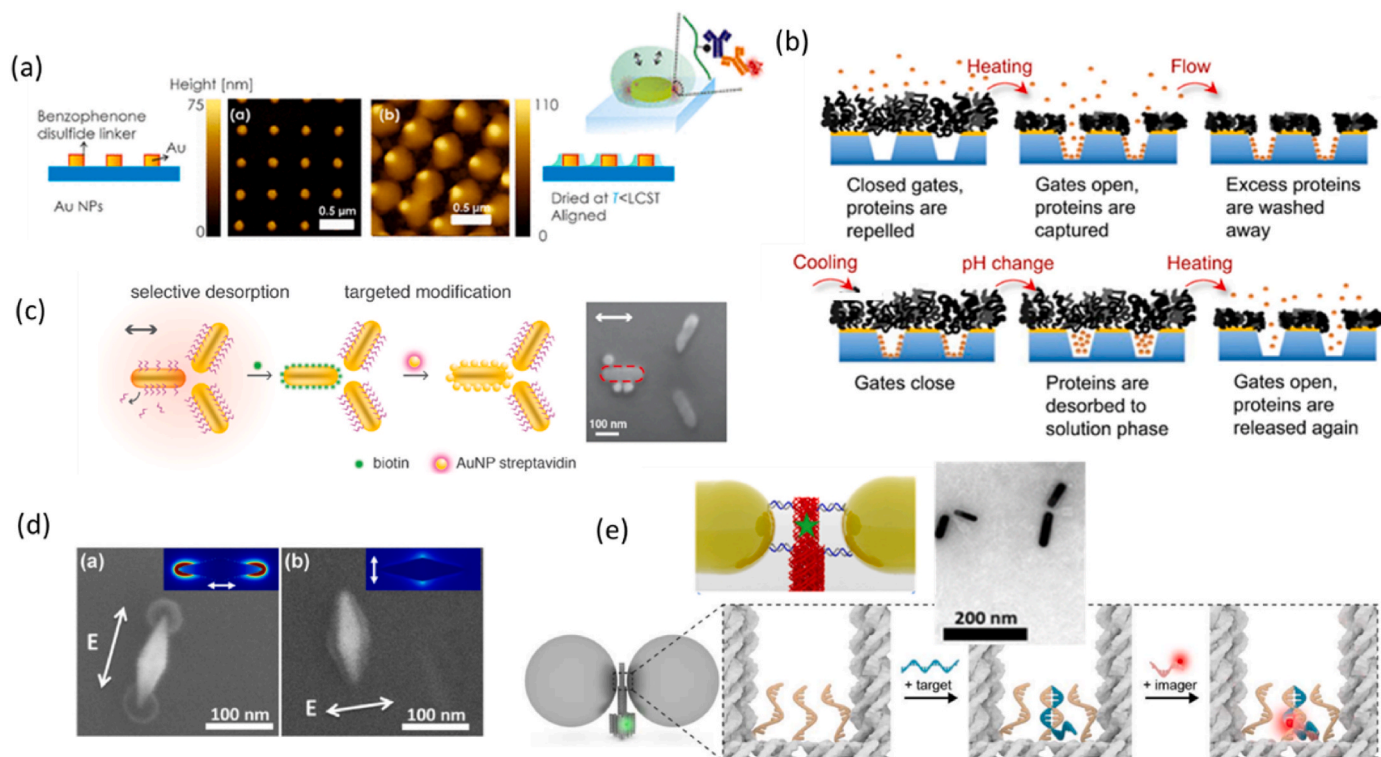

Fig. 6. Examples of explored routes for the selective functionalization of metallic nanostructures based on a) photo-attachment with interference UV interference field pattern overlaying Au nanoparticle arrays (reproduced with permission from Ref. [84] American Chemical Society), b) actuating of plasmonic nanopores for diffusing biomolecules with grafted from responsive pNIPAAm-based brushes (reproduced with permission from Ref. [85]), c) using locally ejected hot electrons for deprotecting selected areas (reproduced from Ref. [86] with permission from the Royal Society of Chemistry). d) Plasmon-enhanced photochemistry (reproduced from Ref. [87] with permission from American Chemical Society), and e) DNA origami scaffolds (reproduced with permission from Ref. [90]).

4.2. Repelling of fouling and control of the distance from the metallic surface

Emitters serving as reporting molecules in PEF assays need to be placed at an optimum distance *f* from the metal surface. As illustrated in the previous section 3, efficient fluorescence signal amplification requires balancing between the effect of quenching occurring at short distances $f < 15$ nm (see Fig. 2) and coupling with surface plasmons with field intensity reaching its maximum at the metallic surface and rapidly decaying into the adjacent dielectric medium (see Fig. 4). These constraints should be taken into account when designing the biointerface of metallic nanostructures and besides the accurate distance *f* providing optimum *EF* it has to allow immobilizing of sufficient amounts of BREs and sustain the ability to repel other molecules present in the analyzed liquid sample. This part focuses on a subset of biointerface architectures, which reflect these three requirements.

For probing with LSPs, the enhanced electromagnetic field intensity occurs at a distance range comparable to the size of the biomolecules (e. g., see the gap size of 11 nm showed in Fig. 6e for the plasmonic nanoparticle dimers in comparison to the hydrodynamic radius of about 5 nm for IgG molecules). This leads to the requirement of using very thin linker layers for the immobilization of BREs. Most commonly, such linker layers are prepared by self-assembly of thiol molecules on metallic surface. These SAMs exhibit a thickness of several nanometers and thiols with PEG headgroups become widely used materials for preparing coatings for suppressing protein sorption due to its excluded volume effect and the dynamic motion of the hydrophilic chain. Thiol SAMs are often used in a mixed format with additional molecules bearing carboxyl or biotin headgroups for coupling of BREs. It is worth noting that other chemical toolkits for thiol SAMs have been recently developed with alternative headgroups such as zwitterionic carboxybetaine and sulfo-betaine units [91] (see Fig. 7a) that have been frequently used in more advanced antifouling materials [92]. Because of strong ionic solvation and charge balance, zwitterionic materials enable the formation of a continuous and tight hydration layer at interfaces to effectively repel the non-specific adsorption.

Another class of biointerfaces relying on 'grafted from' polymer brush architecture was shown to offer improved antifouling properties in plasmonic biosensors when compared to thiol SAMs [93]. These coatings can act as efficient three-dimensional matrices with a thickness of several tens of nanometers and therefore they are suitable for PEF formats relying on the probing with PSPs exhibiting more extended profile of electromagnetic field than LSPs (see Fig. 2). The utilization of PEF for the detection of biomolecules present in complex samples such as saliva was reported with the use of poly[(N-(2-hydroxypropyl) methacrylamide)-co-(carboxybetaine methacrylamide)] copolymer brush that was grafted from the Au surface forming a layer with the thickness 81 nm in the swollen state [65] (see Fig. 7b).

Interesting types of antifouling polymer binding matrices are prepared from responsive crosslinked polymer networks [94]. These networks can take the form of thin hydrogel layers attached to the metallic sensor surface and they can be toggled between swollen and collapsed states. Arguably, the most prominent responsive polymer is pNIPAAm as it exhibits attractive thermoresponsive properties due to its local critical solution temperature (LCST) at around 32 °C. Its copolymers were synthesized for the preparation of three-dimensional binding matrixes with thickness extended $> 10^2$ nm in the swollen state [95] that is far above the probing depth of surface plasmon waves. However, by triggering the collapse of the polymer network by increasing the temperature of the LCST, affinity-captured molecules can be compressed at the metallic surface and thus open the door for increased efficiency of PEF readout through compacting them at the optimum distance *f* [84], see Fig. 7c. Importantly, the magnitude of the collapse in the pNIPAAm-based binding matrix depends on the surface mass density of BREs, and therefore using low molecular weight BREs such as short peptides offers the advantage in this concept [82].

4.3. Assay formats and cyclic reaction amplifications

In PEF affinity-based biosensors, BREs including ssDNA, antibodies, aptamers, and peptides are employed to specifically interact with the target analyte species present in analyzed liquid samples. Target analyte molecules are typically not fluorescent themselves and therefore there are used detection BREs that are conjugated with fluorophore tags. When interacting with the target analyte, a plasmonically enhanced fluorescence signal can be generated by several means. A direct assay
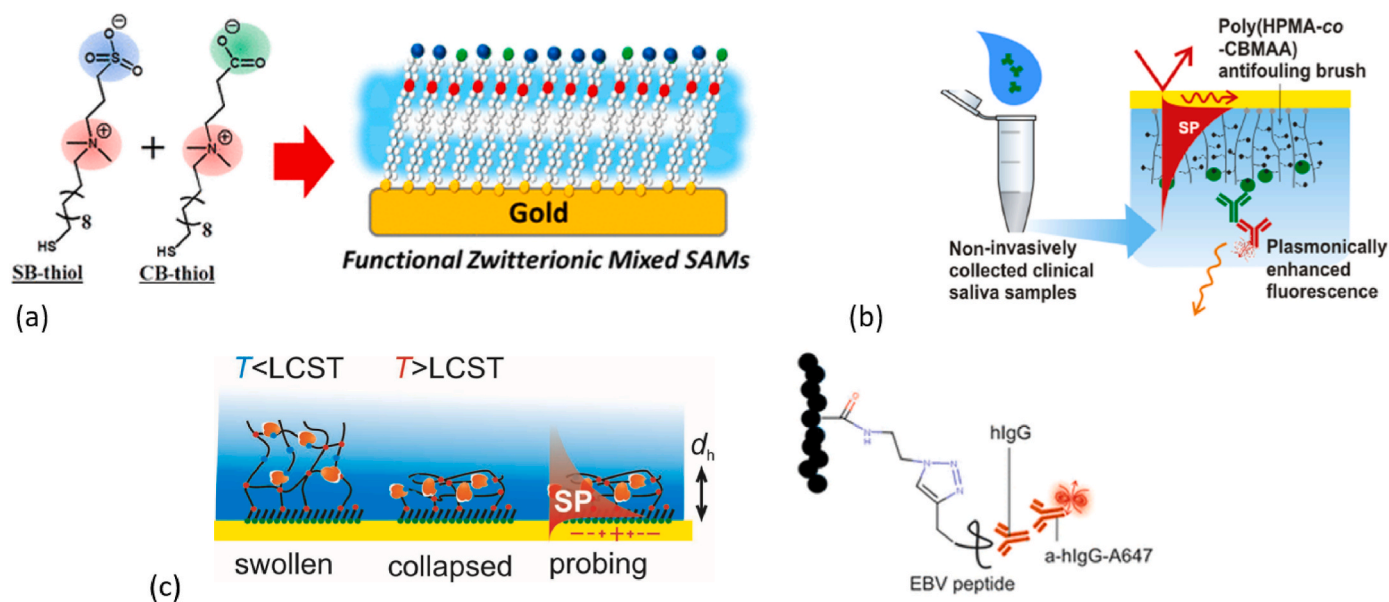

Fig. 7. Examples of routes for functionalization with controlled distance of affinity captured target molecules from the metallic sensor surface by using a) several nanometers thick thiol self-assembled monolayers (reproduced from Ref. [91] with permission from American Chemical Society), b) several tens of nanometers thick biofunctional antifouling polymer brushes (reproduced from Ref. [65] with permission from American Chemical Society), and c) and responsive polymer networks postmodified with biofunctional moieties featuring actuated thickness d_h that can exceed 100 nm (reproduced with permission from Ref. [82]).

format can be implemented by using fluorophore-tagged BREs that upon the capture of the target analyte change their conformation [96,97]. Otherwise, there are commonly used assays relying on multiple reaction steps based on direct sandwich [98,99], indirect sandwich [99–101] or indirect [102,103] and competitive [80] formats.

Nucleic acids designed to form a hairpin structure with a fluorophore on one end and a quencher at the other end of the strand, so-called molecular beacons (MBs), were commonly employed in PEF assays with direct detection format [96,97]. In the closed state of the hairpin, the molecule is turned "off" and a weak fluorescence signal is detected. Upon binding of the target analyte, the hairpin structure is opened and the quencher is separated from the fluorophore tag leading to an increased "on" fluorescence signal. Such an approach has been implemented for the detection of nucleic acid analytes and by using a hairpin aptamer also other low molecular weight molecules can be detected [51]. When immobilized at a close proximity to a metallic surface, the metal can act as a quencher as it strongly changes the quantum yield of fluorophores in a distance-dependent manner (see Fig. 4).

In immunoassays, antibodies are used as BREs and a sandwich format is frequently used [80,104]. A capture antibody is then immobilized on the sensor surface to affinity bind the target molecule from the liquid sample contacted with the sensor surface. Afterwards, the surface is reacted with fluorophore-labelled detection antibodies binding to another part of the captured analyte, and the fluorescence signal (that increases with the analyte concentration) is measured. The indirect sandwich immunoassay, which has a capture antibody on the substrate, a detection antibody reacting with the captured target analyte, and a fluorophore-tagged secondary antibody providing the signal is commonly adopted with PEF [105]. The advantage is that using tagged secondary antibodies (instead of directly tagging detection antibodies as done in a direct sandwich assay) can offer simplification in multiplexed formats. The other prevalent sandwich assay formats utilize aptamers [106], ssDNA [107], or RNA (ssRNA) [108], instead of antibodies as recognition elements.

When employed for the readout of fluorescence assays serving for sensitive detection of chemical and biological species, PEF can be combined with other strategies further improving the sensitivity by associating the presence of target analyte with an increased amount of fluorophore labels. Both enzyme-based and enzyme-free approaches were investigated in combination with optical PEF amplification. Rolling circle amplification (RCA) was employed with PEF for the analysis of nucleic acid and protein analytes. In this method, a short ssDNA tag is hybridized to a circular ssDNA called a padlock probe. This short oligo acts as a primer and it is extended by reacting with the polymerase enzyme in the presence of nucleotides. Long ssDNA strands with the repeating sequences complementary to the padlock are synthesized and they can serve for docking of large amounts of fluorophore-conjugated complementary short ssDNA oligos [79,109]. Another approach for signal amplification is the implementation of cyclic fluorescence probe cleavage, in which the DNA strand is cleaved by an endonuclease to thermo-plasmonically release the fluorescent probes regenerating the target analyte on the surface [110].

In order to develop more robust amplification schemes, efforts were devoted to the development of enzyme-free approaches and catalytic hairpin assembly (CHA) is a prominent example in this research direction. Two DNA hairpins are designed to be opened by strand displacement when a specific trigger sequence is introduced in order to form a complex. When the first hairpin is opened by the trigger, it discloses a ssDNA sequence serving as a toehold for reacting with the second hairpin, which leads to the release of the trigger sequence, making it available for the next reaction cycle. Such reactions were frequently proposed for replacing enzyme-based RCA [111] and in combination with PEF allowed to reach single molecule detection sensitivity [112]. CHA was also advanced to form dendrimers, branched structures, and DNA walkers [113,114]. In addition, a similar approach was reported in combination with DNAzymes for the cleavage of strands to prepare the

gold nanoparticles that initiate the CHA engineered to take place at DNA tetrahedrons [115]. The CHA was also used in PEF-based read-outs for precise imaging *in vitro* and *in vivo* [116].

5. Applications in disease diagnostics

Sensitive analysis of biomarkers and harmful biological compounds become irreplaceable means for early disease diagnosis, guiding of treatment as well as for disease relapse monitoring. However, detection of relevant biomarker targets remains often challenging due to their low quantity and presence in complex biological samples. To detect the targets that are often present at concentrations in the femtomolar concentration range or below, PEF-based platforms have been pursued for improving the limit of detection (LOD) of developed fluorescence assays. This chapter aims to present the recent PEF-based biosensing studies and illustrate the variety of signal-enhancing plasmonic nanostructures and biorecognition mechanisms that are able to detect minute amounts of analytes associated with a wide spectrum of diseases, including cancer, parasitic, viral, and bacterial infections, and neurodegenerative diseases.

5.1. Cancer biomarker analysis

PEF-based biosensing platforms have been widely explored for the detection of biomarkers related to numerous types of cancers, see Table 2. Early detection of cancers is of paramount importance since it is one of the most common causes of death worldwide [117]. In the context of liquid biopsy, there are pursued tools where PEF contributes to delivering ultralow LOD in conjunction with non-invasive means of sampling of bodily fluids (e.g. blood serum or plasma) in which the target biomarkers circulate.

Exosomal miRNAs (exomiRs) are regarded as a potentially rich reservoir of biomarkers for early-stage cancer diagnosis, and they can be simply isolated from serum or urine. For this purpose, the Au nanorods (AuNRs) were drop-casted on Ag-island film, and the capture antibody was attached to the surface via amine coupling [100]. Such solid substrate was used to identify the exosome membrane marker, CD63, in an indirect sandwich immunoassay (Fig. 8a) with Alexa Fluor 647-tagged secondary antibody and microarray scanner readout. This work reported on 360-fold fluorescence enhancement compared to the glass substrate and the detection limit of 0.3 ng/mL was achieved. When the immunocomplex was injected into the plasma samples collected from patients with liver cirrhosis, hepatocellular carcinoma, and two healthy donors, increased secretion of exosomes allowed for the distinction of cancer patients from the healthy controls.

Besides exomiRs, cell-free miRNAs circulating in bodily fluids or the miRNAs that can be obtained from cell lysates are also recognized as biomarkers for the diagnosis of cancers at early stages. miRNA-210 and miRNA-21 have been found to be up-regulated in several kinds of cancer diseases including colorectal and breast cancer [118–120]. Their analysis was reported by using flower-like Ag nanoparticle (FLS)-enhanced fluorescence/visual bimodal readout with increased sensitivity and multiplexed format [121]. The FLS layer was grown on the surfaces of cellulose fibers, microfluidic paper-based analytical devices (μPADs), and then nitrogen-doped carbon nanodot-functionalized DNA1 (DNA1-N-CDs) was physically absorbed into FLS- μPADs. DNA2-CeO$_2$ was added as a fluorescence quencher after the hybridization of DNA1 and DNA2. When the miRNAs were present in the cell lysates, DNA2 bearing the quencher hybridized with the miRNAs leading to the fluorescence recovery. The advantage is the surface can be regenerated and used up to three times after rehybridization of DNA1-N-CDs and DNA2-CeO$_2$. The LODs were 30 aM and 60 aM for miRNA-210 and miRNA-21, respectively.

In order to detect miRNA-21, which is overexpressed in numerous types of cancers, a nanogap antenna was fabricated as a highly sensitive sensing element by using two AuNR-conjugated hairpins H1 and H2

Table 2
PEF-based biosensors detecting cancer biomarkers.

| Target analyte	Cancer type	Plasmonic structure	Biorecognition mechanism	LOD	Ref.
Exosomes in human plasma	Multiple types	AuNRs on Ag island film	Indirect sandwich immunoassay	0.3 ng/mL	[100]
miRNA-210	Colorectal, Breast	Flower-like AgNPs on cellulose fibers	DNA/miRNA hybridization	30 aM	[121]
miRNA-21				60 aM	
miRNA-21	Breast	Colloidal AuNRs nanoantennas	DNA/miRNA hybridization	97 aM	[122]
miRNA-21	Breast	AuNPs adsorbed on magnetic microparticles	RNA/RNA hybridization	9 fM	[123]
PCA3 sequence	Prostate	AuNRs satellite structure	DNA/DNA hybridization	1.4 pM	[124]
CA 19-9	Pancreatic	Au nanotriangular arrays on glass	Indirect sandwich immunoassay	7.7×10^{-7} U/mL	[101]
BRCA-1	Breast	Colloidal AuNPs	ssDNA cleavage by CRISPR-Cas12a	0.34 fM	[125]
Caspase-3	Multiple types	Colloidal AuNPs	Peptide cleavage	10 pg/mL	[127]
ERBB2 gene	Breast	Nanoporous Au disk	DNA/DNA hybridization (MB)	2.4 zmol	[97]
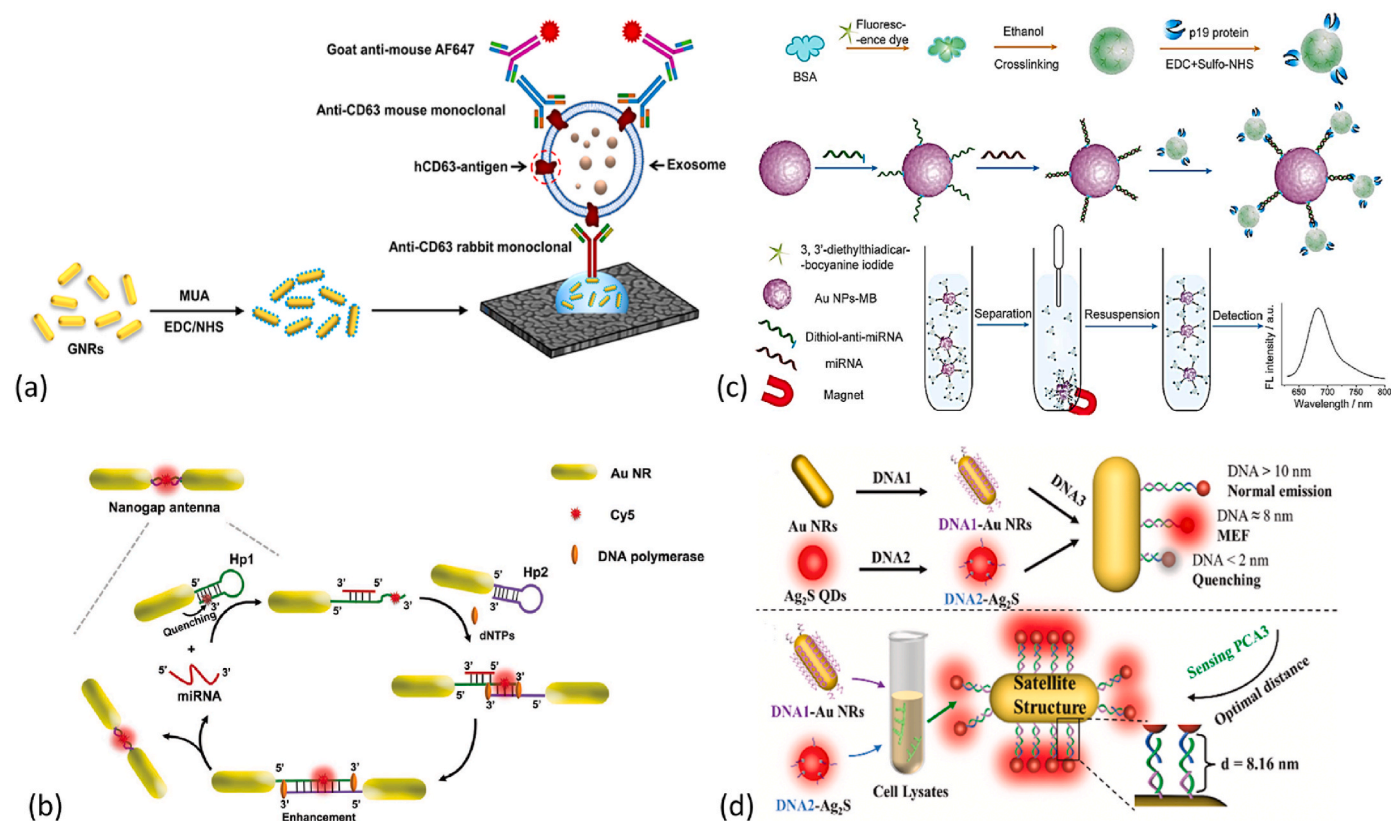
Fig. 8. Schematic illustrations of PEF-based cancer biosensing platforms detecting a) exosomes in plasma samples by targeting exosomal membrane marker CD63 in an indirect sandwich assay performed on AuNRs drop-casted on Ag island film (reproduced from Ref. [100] with permission from American Chemical Society), b) miRNA-21 detection by DNA/miRNA hybridization and fluorescent signal enhancement by the AuNR nanogap antennas (reproduced from Ref. [122] with permission from WILEY-VCH Verlag GmbH & Co. KGaA, Weinheim), c) AuNP-magnetic beads and fluorescent-tagged albumin conjugated to p19 for the detection of miRNA-21 (reproduced from Ref. [123] with permission from Elsevier B.V.), d) PCA3 detection by using NIR-tagged QDs and AuNRs (reproduced from Ref. [124] with permission from Elsevier B.V.).

present in a liquid solution [122]. The presence of the target - breast cancer-associated miRNA-21 - triggers the Cy5-labelled H1 to unfold due to the hybridization with miRNA-21, leading to fluorescence enhancement, and followed by the dimerization of two hairpin structures, see Fig. 8b. In the presence of dNTPs and the polymerase, miRNA-21 is then displaced to catalyze the next reaction, the hairpin structures are elongated, and the fluorescent signal is further amplified by the two AuNR dimers. With this technique, an ultralow LOD of 97.2 aM was reached. For detecting the same miRNA, AuNPs-magnetic beads were prepared by adsorbing the negatively charged AuNPs onto the aminated positively charged surface through electrostatic interactions, and single-stranded RNA (ssRNA) complementary to the target was immobilized onto the Au surface [123]. Additionally, a fluorescent dye (DTDI)-tagged albumin was conjugated to a viral protein, p19, which possesses the ability to recognize double-stranded RNA (dsRNA). In the

presence of miRNA-21 in human serum and MCF-7 cell lysates, hybridization with the complementary ssRNA sequence occurs and the p19 protein binds to the formed dsRNA (Fig. 8c). This magnetic fluorescence miRNA sensing strategy yielded a broad detection range from 10 fM to 10 nM, with a detection limit of 9 fM. A similar detection strategy was utilized with varying lengths of DNA sequences as a biological spacer to precisely regulate the distance between NIR QDs and AuNRs for the detection of prostate cancer marker PCA3 sequence [124]. Both QDs and the AuNRs were modified by ssDNA chains (DNA1 and DNA2) with sequences designed to simultaneously hybridize with the PCA3 DNA sequence, facilitating the signal enhancement (Fig. 8d). The sensor was able to detect the biomarker in human serum samples, and the cell lysates of prostate cancer cell lines PC-3 and LNCap with an LOD of 1.42 pM.

Carbohydrate antigen 19-9 (CA 19-9) is a biomarker associated with

pancreatic cancer. It is one of the most aggressive and lethal cancer types and to increase the very low chance of survival, this disease needs to be diagnosed at a very early stage. To this end, a highly sensitive near-infrared fluorescence immunoassay was developed by using a sensor chip with Au triangular nanoparticle arrays prepared on a solid substrate by colloidal lithography technique followed by functionalizing with anti-CA 19-9 monoclonal antibodies [101]. The indirect sandwich assay with a DyLight 800-conjugated secondary antibody allowed reaching an LOD of 7.7×10^{-7} U/mL in serum samples.

By using CRISPR-Cas12a providing a unique *trans*-cleavage effect, a sensitive and rapid sensor was developed to detect a cell-free DNA (cfDNA) that is related to breast cancer. First, an overhanging DNA bridge was established between spherical Au nanoparticles (AuNP) with a diameter of 20 and 60 nm [125]. While the double-stranded end was conjugated to the 20 nm AuNP, the single-stranded part, which is recognized by CRISPR-Cas12a, was attached to the 60 nm AuNP (Fig. 9a). The shorter sequence of the overhanging DNA is tagged with FITC, at a distance of 2 nm and 7 nm from 60 nm to 20 nm AuNP, respectively. In the presence of breast cancer biomarker - the BRCA-1 gene - CRISPR-Cas12a complex was activated by the hybridization of the BRCA-1 gene with the complementary CRISPR RNA (crRNA) and to cut specifically the ssDNA. This annihilated the fluorescence quenching effect of 60 nm AuNP while unveiling the PEF effect of 20 nm AuNP. It was reported that the LOD of the system could reach down to 0.34 fM. This approach based on PEF in liquid solution overcomes the need for pre-amplification-based approaches which are costly and time-consuming.

Caspases are proteolytic enzymes that play a critical role in homeostasis and apoptosis. Dysregulation of caspases can be attributed to several severe diseases including cancer, inflammatory disorders, and neurodegenerative disorders [126]. Among these, caspase-3 is the central regulatory protein, and its detection was reported by bifunctional AuNPs conjugated with fluorescein isothiocyanate (FITC) via two strands - ssDNA and a peptide [127]. These double bridges were utilized for rapid and sensitive detection of the target analyte by using a peptide sequence than the ssDNA to keep the fluorophore quenched in close proximity ($f < 2$ nm) to the AuNP (Fig. 9b). Once the caspase-3 is present in the sample, it degrades the peptide resulting in an increase in the fluorescence signal due to the elevated distance f to 7–8 nm where PEF dominates over the quenching. The LOD of this solution-based assay was at the caspase-3 concentration of 10 pg/mL.

Epidermal growth factor receptors (ERBB) affect cancer malignancy since they are often overexpressed in various cancer types. The ERBB2

gene codes for a transmembrane protein of this receptor family and it can be targeted as a biomarker molecule. MB probes were immobilized on a nanoporous Au disk, producing a fluorescence signal upon hybridization to the targeted complementary sequence. The sensor was able to detect as low as 2.4 zmol of DNA [97].

5.2. Infectious diseases

As summarized in Table 3, a range of viral and bacterial infections were detected by PEF-based biosensing platforms. PEF was used to detect interleukin 6 (IL-6) that relates to the response of the immune system to infections, a highly stable fluorescent nanoconstruct with high brightness was engineered to boost the fluorescence signal strength NIR fluorophore (800CW, LI-COR) used as a label [104] (Fig. 10a). This nanoconstruct has an AuNR plasmonic nanostructure for fluorescence enhancement, a polymer spacer shell to optimize the distance, and bovine serum albumin (BSA) conjugated with 800CW as light emitter. The whole nanoconstruct coated with BSA-800CW-biotin was utilized as bright label in fluorescence-linked immunosorbent assay (FLISA). For pro-inflammatory cytokine IL-6 an LOD of ~1 fM was achieved, which was enhanced by 4.8×10^3-fold compared to conventional FLISA. Alternatively, the same sensitivity as the conventional FLISA was reached but with greatly shorten assay time (20 min compared to 280 min). The same nanoconstruct was also used for the development of ultra-sensitive lateral flow immunoassay (LFIA) to detect SARS-CoV-2 and IL-6 in human plasma, SARS-CoV-2 antibody in human serum, and SARS-CoV-2 antigen nucleocapsid in nasopharyngeal swap samples [128]. In comparison to the conventional AuNP-based LFIAs, an improvement in LOD by a factor of 1.8×10^3-fold for IL-6, 5.7×10^2-fold for the SARS-CoV-2 antibody, and 400-fold for the nucleocapsid was achieved. When the method was compared to the standard sandwich ELISA, a 30-fold increase in LOD for IL-6, a 165-fold increase for SARS-CoV-2 antibodies, and a 37-fold increase for nucleocapsid have been observed. This work demonstrates that PEF employed in lateral flow devices can also significantly improve the performance of this widely spread and established platform providing enhanced sensitivity, accuracy, and faster results compared to traditional tests.

SARS-CoV-2 was also successfully detected by amplification techniques such as thermoplasmonic-assisted cyclic cleavage for viral DNA detection. Upon binding of the target sequence on ssDNA modified Au nanoisland attached to the solid sensor surface, fluorophore-labelled ssDNA strands were bound on the free end of the target molecule, which was then cleaved by endonucleases to release the dyes and
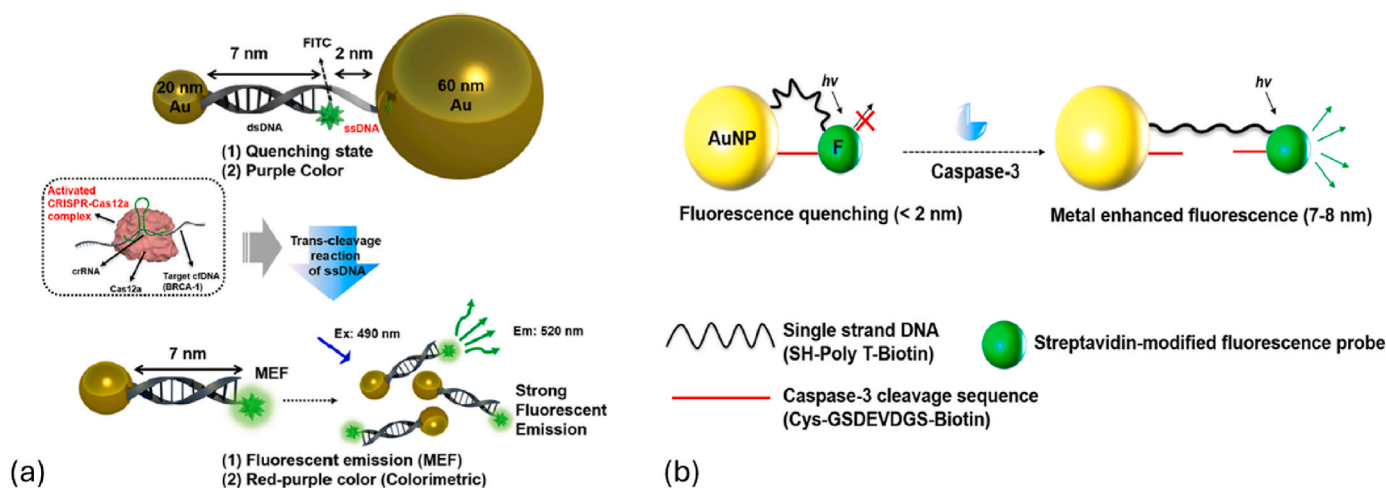

Fig. 9. Schematics of PEF platforms for the detection of a) cell-free DNA (cfDNA) by activating CRISPR-Cas-12a and AuNPs functionalized with DNA (reproduced from Ref. [125] with permission from American Chemical Society), b) caspase-3 by using AuNP functionalized with ssDNA and a caspase-3 target peptide sequence having a fluorescent tag (reproduced from Ref. [127] with permission from American Chemical Society).

Table 3

PEF-based biosensors detecting biomarkers of parasitic, viral, and bacterial infections [104].

| Target analyte	Disease	Plasmonic structure	Biorecognition mechanism	LOD	Ref.
Interleukin 6	Inflammation	AuNR	Sandwich immunoassay with PEF label	1 fM	[104]
Interleukin 6	Inflammation	Au films	Sandwich immunoassay with RCA	4.3 fM	[109]
Human antibody against spike antigen	COVID-19 infection	Ag-coated AuNR plasmonic nanoantenna	Indirect sandwich immunoassay	185 pg/mL	[128]
Nucleocapsid antigen				212 pg/mL	
VTS-nsp13 viral target sequence	COVID-19 infection	Au nanoislands	DNA/DNA hybridization (amplification-based cyclic fluorescence probe cleavage)	0.28 fM	[110]
N gene	COVID-19 infection	Conical Au nanoarray on SiO$_2$ sheets	DNA/DNA hybridization (reverse transcription-enzymatic recombinase amplification)	28 copies/mL	[129]
ORF1ab gene				23 copies/mL	
Plasmodium falciparum lactate dehydrogenase	Malaria infection	AuNPs on the glass substrate	Direct sandwich assay with capture antibody and detection aptamer	18 fM	[130]
Human IgG, IgM	Lyme disease	Au-coated silicon microchip	Indirect immunoassay	Not specified	[103]
Human IgG, IgA IgM	*Toxoplasma gondii* infection	Au nanoislands	Indirect immunoassay	Not specified	[134]
HIV DNA	AIDS	AuTNPs	DNA/DNA hybridization (CHA)	0.83 fM	[132]
16S rRNA	Staphylococcal food-born disease	AuNPs	DNA/DNA hybridization (CHA)	9.0 fM	[102, 114]
EBOVgp-Fc sGP	Ebola virus disease	Au nanoantenna array on a glass substrate	Indirect sandwich immunoassay	5.6 pg/mL	[99]
				11 pg/mL	
rHA	Avian influenza	Core-shell Ag NP	G-quadruplex aptamer	3.5 ng/mL	[106]
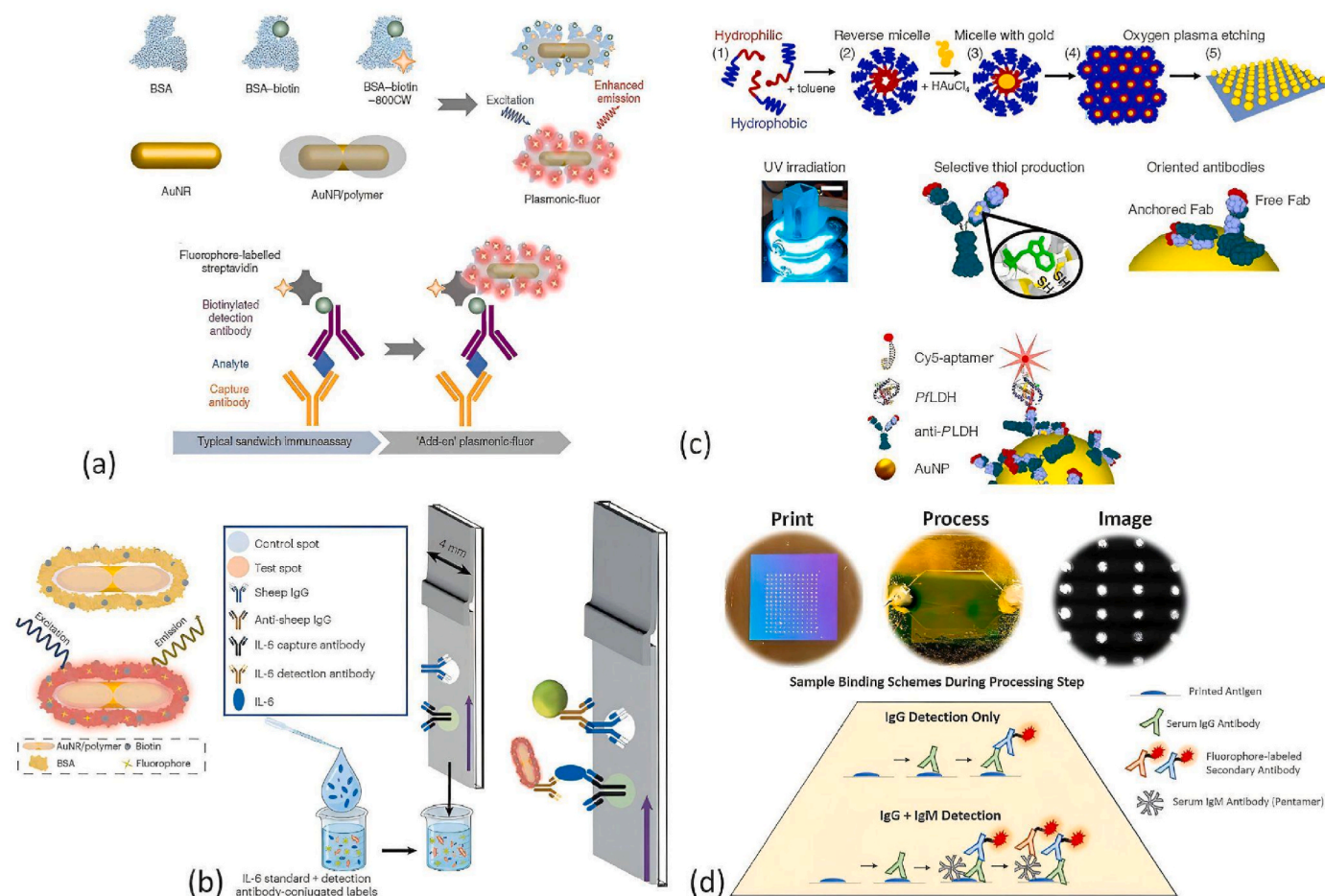
Fig. 10. Schematic representations of a) IL-6 detection in an indirect sandwich assay by enhancing the signal by using the plasmonic fluorescent label (reproduced from Ref. [104] with permission from Springer Nature), b) SARS-CoV-2 nucleocapsid antigen, and human antibodies in serum against SARS-CoV-2 spike antigen detection with LFIA using the plasmonic fluor (reproduced from Ref. [128] with permission from Springer Nature), c) malaria biomarker PfLDH by using AuNPs synthesized by block copolymer micelle nanolithography (BCMN) in a sandwich assay having capture antibody and detection aptamer (reproduced with permission from Ref. [130]), d) human IgGs/IgMs in an indirect assay by using the grating-coupled fluorescent plasmonic technique (reproduced with permission from Ref. [103]).

dehybridize via thermoplasmonic heating in order to produce a strong fluorescence signal. The sensor can be used for multiple cycles, achieving the LOD of 0.275 fM for the tested VTS-nsp13 sequence, and showed rapid and reliable performance also in clinical settings [110]. A point-of-care device for two genes found in SARS-CoV-2 was developed with an isothermal amplification reaction based on enzymatic recombinase amplification advanced by gold nanoarray structure. The sensor was validated with clinical samples, showing LODs of 28.3 copies/mL for the N gene and 23.3 copies/mL for the ORF1ab gene [129].

The PEF-based biosensing platforms were exploited for the diagnosis of vector-borne diseases caused by parasites including malaria, which remains one of the most life-threatening diseases in tropical countries with limited access to appropriate storage and transportation capacities. To achieve the ultrasensitive detection of a malaria biomarker *Plasmodium falciparum* lactate dehydrogenase (PfLDH), substrates with Au nanostructure were prepared by block copolymer micelle nanolithography (see section 3.3) [130]. On top of this substrate, capture antibodies were immobilized in the orientation controlled by using the photochemical immobilization technique. The capture antibody was exposed to PfLDH-spiked human blood and then the sensor surface was contacted to a solution with dissolved Cy5-tagged PfLDH detection aptamer forming a sandwich (Fig. 10c). The fluorescence readout signal was measured with a fluorescence microscope and an LOD of 18 fM was reported to be achieved. Another vector-born infection with *Borrelia burgdorferi,* which is the main cause of Lyme disease, was similarly detected by a protein microarray biochip with plasmonic grating-coupled fluorescence functionality [103]. The positive and the negative control antigens were attached to Au-coated silicon microchips having a plasmonic diffraction grating (Fig. 10d) and reacted with sera from patients in various stages of the disease for multiplex screening of

16 antigens. The plasmon-enhanced fluorescence signal was measured subsequently to the injection of Alexa Fluor 647-tagged detection antibodies in the indirect sandwich assay. Considering the deposited volume of the antigens, spot size, and the molecular weight of the antibody, it was calculated that this platform can reach an analytical sensitivity of 8.5 fmol of IgG per spot.

Toxoplasma gondii is a protozoan parasite that causes the disease toxoplasmosis. Although it is generally asymptomatic, it can cause physical (mostly ocular) diseases and intellectual impairments (hydrocephalus) in congenitally infected children, and encephalitis in people suffering from acquired immune deficiency syndrome (AIDS) [131]. A multiplex assay platform for the serological diagnosis was aimed to detect IgG, IgA, and IgM antibodies during pregnancy [102]. An antigen mixture of *T. gondii* was immobilized on a solid substrate with Au nanoislands by robotic array printing. Then the sensor chip was incubated with human sera or whole blood samples. For the multicolor detection, Cy3-labelled anti-human IgG, IRDye680-labelled anti-human IgM, and IRDye800-labelled anti-human IgA secondary antibodies were used for the indirect immunoassay (Fig. 11a). This multiplexed assay platform performed high specificity and sensitivity and required a very small amount of sample.

Human immunodeficiency virus (HIV) is mostly a sexually transmitted infection that causes AIDS leading to immune failure and remains a prominent global public health issue. For the detection of HIV DNA fragments, a label/enzyme-free approach based on CHA, as introduced in Chapter 4.2, was utilized by tuning the distance between the surface of the gold triangular nanoplates (AuTNPs) and the fluorophore N-methyl mesoporphyrin (NMM) in liquid solution [132]. The sensor takes advantage of two hairpin structures, HP1 having sulfhydryl to attach AuTNPs, and HP2 which is complementary to HP1 (Fig. 11b). In the case
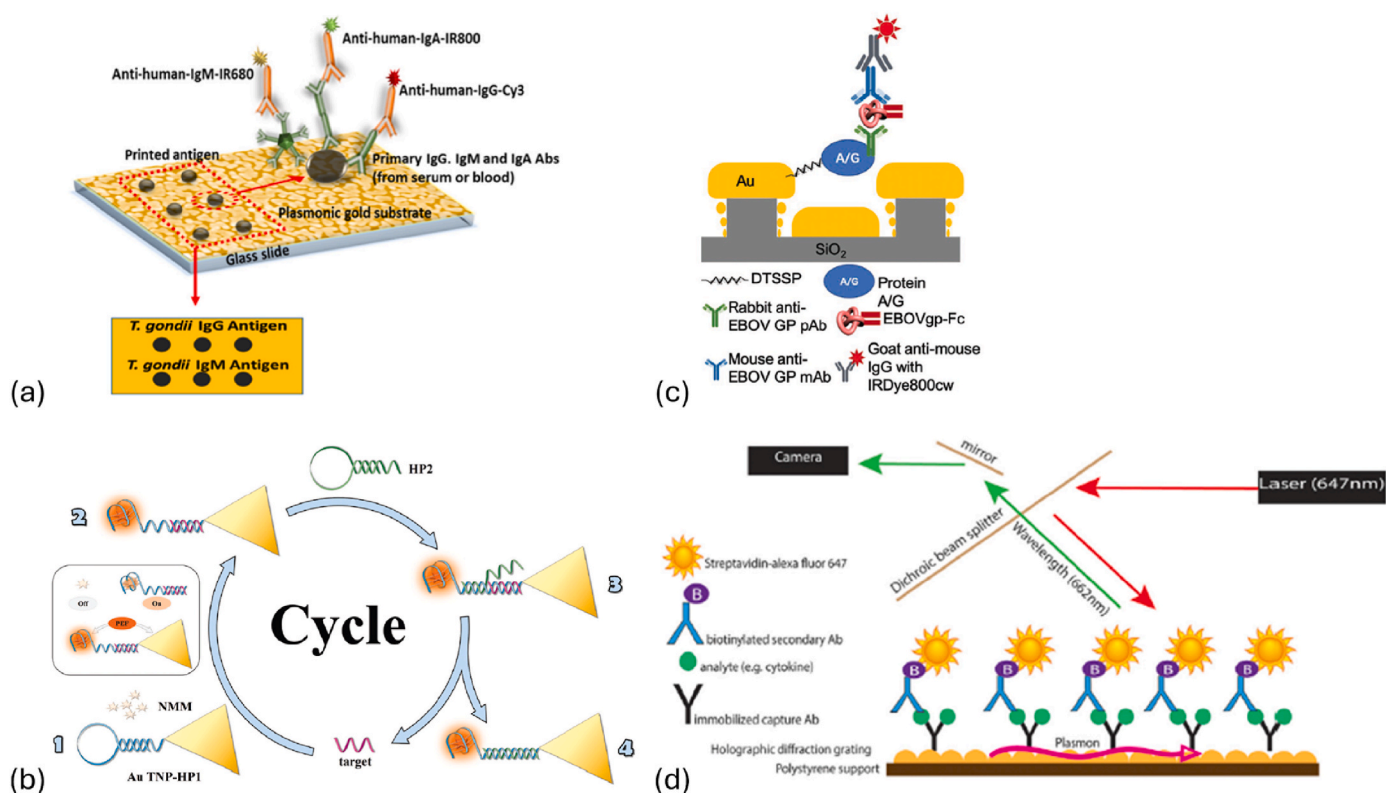

Fig. 11. PEF-based biosensing platforms detecting a) human IgG, IgA, and IgM against *T. gondii* in an indirect assay by immobilizing the specific antigens on Au nanoisland surface (reproduced from Ref. [102] with permission from American Society for Microbiology), b) HIV DNA by using CHA with DNA hairpin immobilized AuTNPs (Reproduced from Ref. [112] with permission from the Royal Society of Chemistry), c) EBOVgp-Fc and sGP antigens of Ebola virus in an indirect sandwich assay on Au nano-discs (reproduced from Ref. [99] with permission from WILEY-VCH Verlag GmbH & Co. KGaA, Weinheim), d) various types of cytokines, chemokines, spike protein in an indirect sandwich immunoassay by immobilizing the specific antibodies on GC-FP Au sensors (reproduced with permission from Ref. [133]).

of target DNA binding, the G-quadruplex region of HP1 is available to interact with *N*-Methyl mesoporphyrin IX resulting significant fluorescence signal increase at 645 nm. After introducing HP2, the HIV DNA is displaced to trigger further cycles of hairpin assembly causing the fluorescent signal amplification, which was reported to allow for reaching LOD of 0.83 fM in human serum samples.

An advanced CHA method with DNA walkers was also implemented for the detection of RNA from the 16S ribosome of *Staphylococcus aureus*, a food-borne pathogen [114]. Colloidal AuNP were capped by a DNA hairpin structure conjugated with a fluorophore label. This fluorophore is quenched in the closed hairpin state due to the close proximity to the Au surface. Another DNA hairpin molecules were present in a bulk solution and in the presence of the bacterium, which causes the surface immobilized hairpin to open, the second hairpin can bind, capable of walking on the AuNP surface to recycle the target. Thus, cyclic reaction leads to the sequential opening of a large number of surface-attached hairpins lifting up the fluorophore labels to a distance where PEF occurs, generating an output fluorescence signal. The method proved better sensitivity than other tested methods with the LOD of 8.96 fM.

Three-dimensional nanoantenna arrays were employed for PEF detection of antigens of the Ebola virus (EBOV), which causes one of the most contagious diseases with a high mortality rate [99]. Nanoantenna arrays were designed using periodic arrays of SiO_2 nanopillars with Au nanodisc on the top and perforated Au film at the bottom (Fig. 11c). This structure was functionalized with a protein A/G serving as a molecular spacer optimized for sandwich immunoassay. The EBOV antigens, Fc fusion of the extracellular domain of EBOV glycoprotein (EBOVgp-Fc), and EBOV soluble glycoprotein (sGP) were detected in the indirect sandwich assay format with IRDye800-labelled secondary antibodies. The LODs of EBOVgp-Fc and sGP in human plasma by using the nanoantenna array sensing platform were found to be 5.6 pg/mL and 10.7 pg/mL, respectively, while ELISA showed notably higher LODs of 37 ng/mL for EBOVgp-Fc and 1 ng/mL for sGP.

Another severe disease with a high death rate is associated with the Avian influenza virus. Point-of-care sensor, which can rapidly detect the recombinant hemagglutinin (rHA) protein derived from the Avian influenza virus subtype H5N1 virus was developed based on PEF [106]. Ag core - SiO_2 shell colloidal nanoparticles served as a substrate for the immobilization of aptamers specific to the target virus protein. Upon interaction with the target analyte, the ssDNA aptamer formed a G-quadruplex that can accommodate thiazole orange and rHA fluorophores generating an enhanced fluorescence signal. This method was reported to achieve the LOD of 3.5 ng/mL in human serum samples.

A grating-coupled fluorescence microarray technology was employed to create biomarker patterns in saliva and serum samples from pediatric patients with multisystem inflammatory syndrome (MIS-C), which is a rare but severe condition that can appear 4–6 weeks after the infection with SARS-CoV-2 [133]. These chips were fabricated in the same way described in the previously discussed study [103] and

modified with capture antibodies to detect a set of 33 analytes, including cytokines, chemokines, spike protein receptors, and markers for tissue damage, cell death, and more, to characterize the biosignatures of pediatric patients with the indirect sandwich assay format (Fig. 11d).

5.3. Other clinical applications

Additional studies explored the implementation of PEF for the analysis of analytes related to other health conditions including cardiovascular and neurological disorders and organ injury as wrapped up in Table 4. Cardiovascular diseases are the leading causes of death globally [135]. Shortly after a heart attack, even if it is without any symptoms, it is possible to detect cardiac troponin I (cTnI) biomarker in the blood as it enters the bloodstream quickly and stays circulating for a couple of days. This analyte was detected by PEF direct sandwich immunoassay with Alexa Fluor 647-labelled detection antibody [136]. ATR in the Kretschmann configuration was used with a light pipe configuration and Fresnel lens - improved collection efficiency of fluorescence light. The capture antibody was immobilized via the protein G fused to ORLA85 protein on a solid substrate with thin Au film. The reported LOD of 0.98 ng/mL was higher than 0.21 ng/mL measured by ELISA, however, due to the pH-tolerant ORLA85, the semi-continuous measurement was possible. In another study, a similar optical configuration was used for cTnI assay with PEF readout, where detection antibody was conjugated to Alexa Fluor 647 in order to specifically recognize the cTnI [80]. Assay performance was investigated for direct, sandwich, and competitive formats with polyclonal and monoclonal antibodies. For the competitive assay, the detection antibody was pre-incubated with a liquid sample before flowing the solution over the sensor surface with immobilized cTnI protein by amine coupling. In this study, an LOD of 19 pM was achieved for a detection time of 45 min.

Traumatic brain injury (TBI) is a common neurological disorder, which can lead to neurodegeneration. Nanosphere lithography was used to construct Au nanopyramid arrays on solid sensor surface that carried an additional thin layer of silica reducing fluorescence quenching. On this PEF substrate there was immobilized capture antibody specific TBI biomarker - glial fibrillary acidic protein (GFAP) [137]. In sandwich immunoassay format, detection antibody labelled with NIR fluorophore Dylight 755 was used yielding plasmonic biosensor detecting GFAP with LOD of 0.6 pg/mL that was improved with respect to ELISA providing LOD of 9.8 pg/mL.

PEF was also employed in assays where metallic nanostructures serve as labels in microarray-based detection platforms [138]. The dendron-modified glass substrate was utilized to immobilize the DNA probe to capture miRNA-134, which is a brain-specific biomarker responsible for neurogenesis/synaptic development and has been demonstrated in previous studies to be associated with diseases such as epilepsy, major depressive disorder (MDD), Alzheimer's disease and frontotemporal dementia [139–141]. Fluorescence-amplifying

Table 4
Overview of PEF-based biosensors detecting biomarkers related to organ injury, inflammation, and neurodegenerative diseases.

Target analyte	Disease	Plasmonic structure	Biorecognition mechanism	LOD	Ref.
Cardiac troponin I	Heart attack	Flat Au film	Direct sandwich immunoassay	0.98 ng/mL	[136]
Cardiac troponin I	Heart attack	Flat Au film	Competitive immunoassay	19 pM	[80]
Glial fibrillary acidic protein	Traumatic brain injury (TBI)	Au nanopyramids on glass	Direct sandwich immunoassay	0.6 pg/mL	[137]
miRNA-134	Neurogenesis-related	AuNRs colloid	DNA/miRNA hybrid detection by indirect immunoassay	1 fM	[138]
KIM-1	Kidney injury	AuNRs attached to PDMS film	Direct sandwich immunoassay	0.5 pg/mL	[66]
miRNA-124	Stem cell neurogenesis	Au/Ni NRs colloid	DNA/miRNA hybridization	Not specified	[96]
Caspase-3	Neurodegenerative disease	AuNP colloid	Peptide cleavage	10 pg/mL	[127]
Interleukin 6	Inflammation, lethal sepsis	Ag-coated AuNR nanoantenna	Direct sandwich assay	362 pg/mL	[128]
Interleukin 6	Inflammation, lethal sepsis	Ag-coated AuNR nanoantenna	Direct sandwich assay	1 fM	[104]
Pyrophosphate	Various genetic diseases	Core-shell Au nanocube	RCA	1.3 pM	[142]
Pyrophosphate	Various genetic diseases	Au nanobipyramid antennas	RCA	80 nM	[143]

nanocuboids (FANCs) with precisely controlled PEF were developed by using AuNRs conjugated with Alexa Fluor 647 via ssDNA linkers and by using an Ag shell. The DNA/miRNA hybrid on the microarray was recognized by a monoclonal antibody reacted with a FANC-tagged secondary antibody (Fig. 12a). A 100-fold higher sensitivity compared to the commercial fluorescence labels was achieved providing a dynamic range from 100 aM to 1 pM.

An alternative approach to amplify the fluorescence readout signal was explored based on contacting fluorophore labels captured on the sensor surface after performing an assay with metallic nanostructures tethered to a flexible polydimethylsiloxane sheet (Fig. 12b) [66]. This element was referred as to a plasmonic patch, and it was used for multiplexed detection of multiple biological targets. By this approach, LOD for the kidney injury molecule-1 (KIM1), which is an early-stage biomarker of acute kidney injury, was ~30 times lower (0.5 pg/mL) than that of ELISA (15.6 pg/mL), and comparing to the unenhanced signal, 36-fold fluorescence enhancement in the plasmonic patch was measured.

Exosome biomarkers carrying miRNA cargo were analyzed with the help of PEF for non-destructive characterizing stem cell neurogenesis [96]. The platform combined selective isolation of exosomes and sensitive miRNA detection by multifunctional magneto-plasmonic nanorod prepared via an anodized aluminum oxide template. These magneto-plasmonic nanostructures were composed of Ni segments conjugated with IgG antibody specific to a membrane marker CD63, and Au plasmonic segment with a fluorophore 5-FAM-labelled ssDNA hairpin (Fig. 12c). The antibodies were used for the capturing of exosomes and their subsequent isolation by applied magnetic field gradient.

After the exosome lysis, released miRNA cargo was detected with the same structure by reacting with the ssDNA hairpin that changed its conformation, and the conjugated fluorophore was switched from quenched to PEF-amplified state. The method was successfully applied to detect neuronal biomarker miRNA-124 in human induced pluripotent stem cell-derived neural stem cells (hiPSC-NSCs) with good linearity ($R2 = 0.98$) at a wide range of concentrations (ranging from 1 pM to 1 μM). With this multifunctional magneto-plasmonic -based approach it is envisaged to be possible to monitor stem cell differentiation in time for future stem cell therapies. Additionally, with this advanced diagnosis technique it can be possible to detect the exosomes as the sources of early-stage cancer biomarkers.

An important byproduct of DNA synthesis is pyrophosphate (PPi), which serves as a target analyte in sensors or for sequencing methods. It was used in PEF sensors for monitoring point mutations, which can be the cause of various genetic diseases. For this purpose, the RCA method, an enzymatic amplification technique (introduced in chapter 4.3), was used to detect the point mutation in the DNA sequence, producing PPi in the process. The detection was employed on the surface of core-shell Au nanocube particles modified with fluorophores with a turn-on and off mechanism based on the high affinity between the byproduct PPi and copper-ions, achieving the LOD of 1.3 pM [142]. The same mechanism was exploited with Au nanobipyramids - fluorescence enhancement of near-infrared dyes, providing a stronger signal when compared to AuNRs, where the fluorescence quenching is induced by copper-ions for bio-applications with the LOD of 80 nM [143].
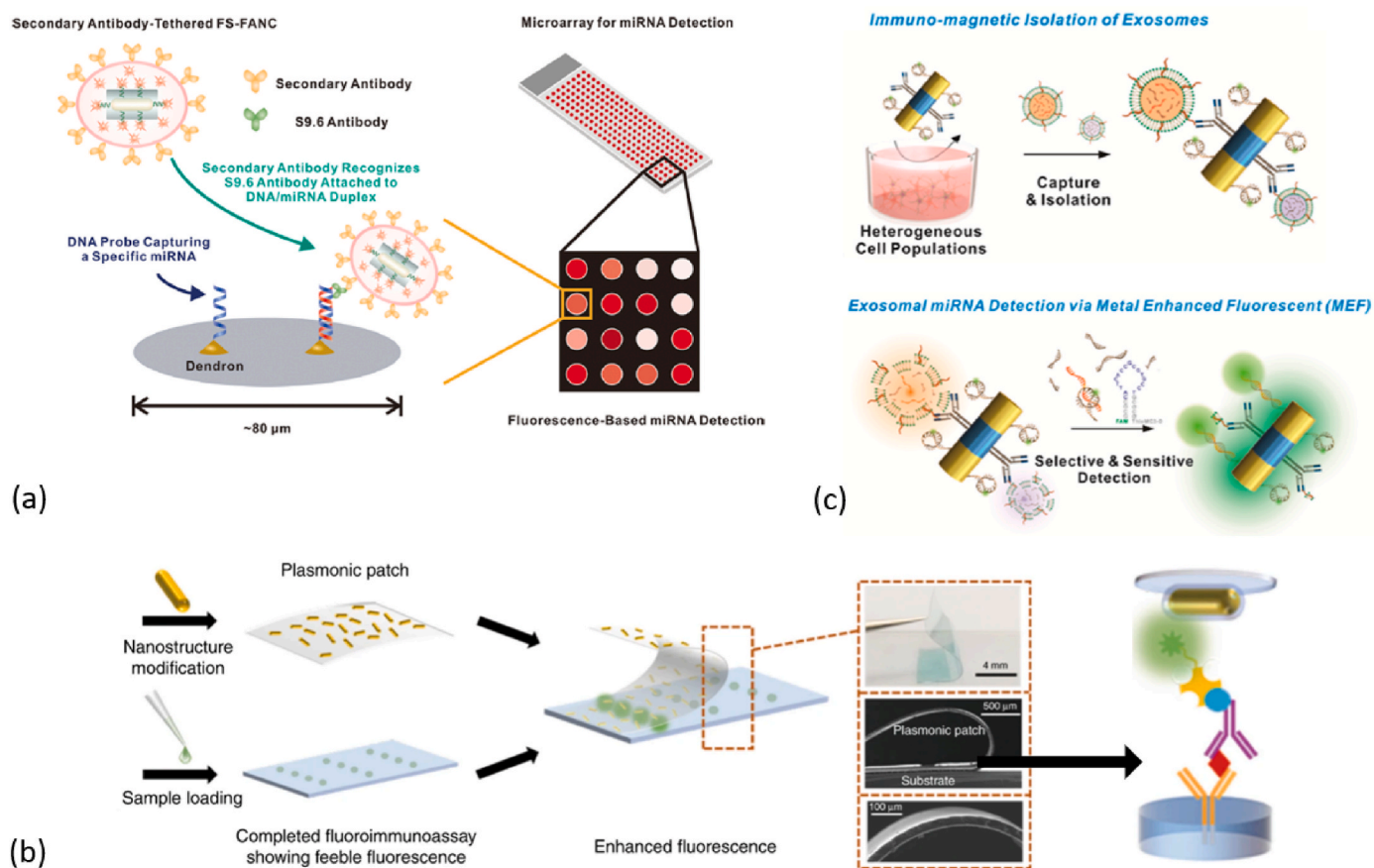

Fig. 12. Schematic illustrations of the PEF-based biosensors detecting a) miRNA-134 with DNA/miRNA hybridization with FANC-tagged secondary antibody on a dendron-modified glass substrate (reproduced from Ref. [138] with permission from American Chemical Society), b) KIM-1 by using a plasmonic patch integrated on the assay surface having fluorescent dye (Reproduced with permission from Ref. [66]), c) miRNA-124 with DNA/miRNA hybridization by using Au/Ni NRs (reproduced from Ref. [96] with permission from American Chemical Society).

6. Applications in cell imaging

Biomolecule imaging gained significant importance in targeting specific biomarkers, such as proteins, nucleic acids, or other biologically relevant compounds that are secreted by cells, located on the cellular surface, or within the cell structure. Biomolecule imaging of individual cells in a population was pursued for identifying cellular heterogeneity (rather than population-averaged measurements) as cellular communications mediated by protein secretion are responsible for important physiological functions, such as metabolic regulation, growth and proliferation, cell-death modalities and immune response [144–146]. Secretomic heterogeneity, referring to as the protein secretions on a cell-to-cell basis in terms of their spatiotemporal distribution [147,148] has been studied to gain an understanding of the inner workings of cellular secretion, for exploring the evolution of dynamic diseases [149], and in developing new pharmacological therapies [150]. These topics were addressed by numerous PEF-based sensor concepts that utilized colloidal metallic nanostructures as discussed in the following section. Moreover, fluorescence microscopy represents a dominantly used method for the imaging of cells and several works explored the use of surface plasmon-based optics for increasing its sensitivity as discussed in the succeeding part.

6.1. Monitoring of intracellular biomolecules with colloidal nanostructures

As summarized in Table 5, PEF-based bioimaging was mainly employed for cancer biomarkers miRNA-21, but also other analytes including miRNA-373 and protein analytes related to telomerase activity and transcription were analyzed in cancerous and non-tumorigenic cell lines. There were reported LODs reaching as low as fM concentrations by a combination of cyclic reaction formats and metallic nanostructures. Au nanostar NP with SiO_2 shell was used for constructing of PEF probe, incorporating 20 symmetrical hotspots to enhance the sensitivity of imaging intracellular miRNAs [151]. By optimizing the thickness of the SiO_2 shell, the 21-fold increase in fluorescence signal was achieved for fluorescently labelled DNA immobilized on Au probe surface. This PEF probe exhibits significantly stronger fluorescence signals compared to traditional plasmonic structures, such as gold nanorods, nanobipyramids, and nanoprisms, due to the high density of hotspots. It surpassed conventional plasmonic structures and provided the LOD of 0.21 pM for miRNA-21 analysis with the use of displacement assay and quenching modulation. Confocal imaging demonstrated its capability to distinguish between cancerous (MCF-7 and HeLa) and normal cells (L02) based on miRNA-21 expression levels, highlighting its potential for *in situ* imaging of miRNAs and serving as a powerful tool for early cancer diagnosis and research. The specificity for detecting miRNA-21 secreted by the cells was assessed by examining its response to commonly co-existing miRNAs, such as miRNA-16 and miRNA-141, as well as other intracellular analytes like carcinoembryonic antigen (CEA) and glutathione (GSH).

PEF-based detection was also demonstrated in living cells by the uptake of Au nanobipyramids functionalized with a fluorophore-tagged hairpin sequence [152]. This hairpin is designed to quench the fluorescence signal of the fluorophore in its closed state by positioning the fluorophore close to the metal. By affinity reaction with the target sequence, the hairpin is opened and fluorescence is turned "on" by lifting up the fluorophore. The principle was used for *in situ* imaging of the activity of telomerase - a ribonucleoprotein, which adds a significant repetitive sequence to chromosomes that is highly expressed in cancer cells. The sensitivity was assessed to be 23 HeLa cells. In another study fluorescent upconversion nanoparticles were linked with Au nanopyramids via two stimuli-responsive DNAzymes, which were combined extracellularly and activated intracellularly via the target sequence even with a recycling mechanism [153]. These authors also introduced a logic gate approach by adding a photo-cleavable linker for blocking of the

Table 5
Overview of PEF-based biosensors for intracellular detection of analytes.

| Target analyte	Cell type	Plasmonic structure	Biorecognition mechanism	LOD	Ref.
miRNA-21	MCF-7, HeLa, L02	Au nanostar	DNA/RNA hybridization	0.21 pM	[151]
APE1 miRNA-21	HeLa, L02	AuNP nanogap antenna	DNA/DNA hybridization	1.8 mU/mL	[154]
				0.34 pM	
miRNA-21	MCF-7, HepG2, L02, malignant MCF-7, metastatic MDA-MB-231, nontumorigenic MCF-10A	Au nanostars	DNA/DNA hybridization	0.26 pM	[155]
miRNA-21	SW48, LoVo	Au-nanodot-decorated hollow carbon nanospheres	DNA/DNA hybridization	0.68 nM	[156]
miRNA-373	HeLa	Au nanopyramid	DNA/DNA hybridization (CHA)	0.48 nM	[116]
c-MYC	MCF-7, HeLa, L02	Au nanopyramids	DNA/DNA hybridization (DNAzymes)	0.35 pM	[153]
Telomerase activity	HeLa	Au nanobipyramids	DNA/DNA hybridization	23 cells	[152]
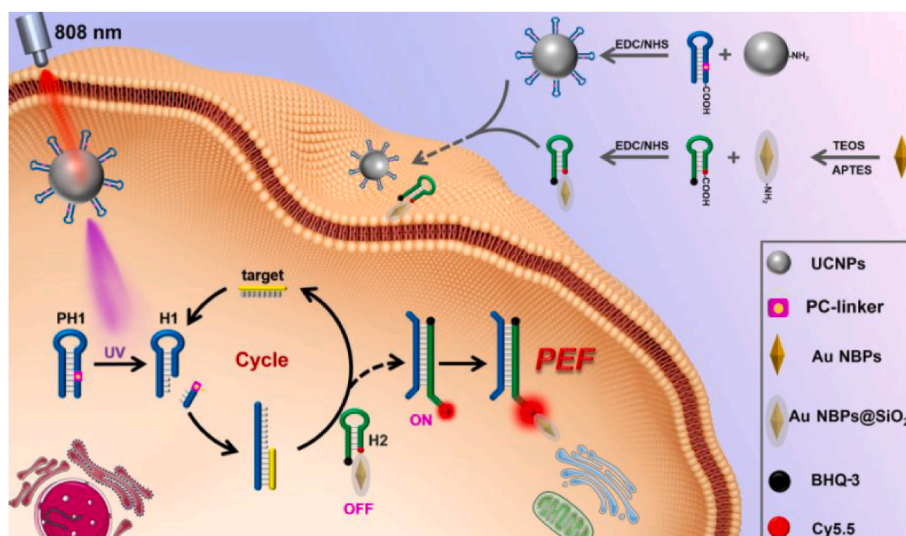
Fig. 13. PEF-based imaging of intracellular miRNA-373 with upconversion nanoparticles (UCNPs), Au nanopyramids (Au NBPs) and CHA. Reproduced from Ref. [116] with permission from American Chemical Society.

sequence. The system achieved an LOD of 0.35 pM for c-MYC, which is a relevant gene in cancer proliferation that is overexpressed. Similarly, this approach, as shown in Fig. 13, was implemented with the CHA as cyclic amplification inside the cells for miRNA-373 with a detection limit of 0.48 pM, also demonstrating the applicability in *vitro* studies with mice [116].

A similar approach was demonstrated for dual sensing of apurinic/apyrimidinic endonuclease 1 (APE1) and miRNA-21 in the HeLa and L02 cell lines [154]. Plasmonic hotspots were created by intracellular assembly of AuNPs forming a nanogap antenna by a combination of cleavage and opening of hairpin structures via the analytes as input in a cyclic format, programming an "AND-gate" mechanism. The achieved LOD was reported for APE1 with 1.8 mU/mL and for miRNA-21 with

0.34 pM. The platform was further advanced to "OR-AND" gates with the first entry point at Mucin 1 located at the membrane for taking into account the cell type for screening of different cancer cells [155]. This work implemented Au nanostar NP structure as previously introduced achieving an LOD of 0.26 pM for miRNA-21.

Another platform for detecting miRNA-21 in SW48 and LoVo colorectal cancer cell lines was developed by using 3–12 nm sized Au NP decorated by hollow carbon nanospheres (AuHCNs) having a diameter of 120 nm and coated with hyaluronic acid (HA) [156]. This design facilitated targeted cellular uptake through CD44 receptor-mediated endocytosis. The platform employed a fluorescence energy transfer (FRET)-based "off-on" fluorescence mechanism, where FAM-labelled ssDNA probes on the AuHCNs are quenched until miRNA-21 binding
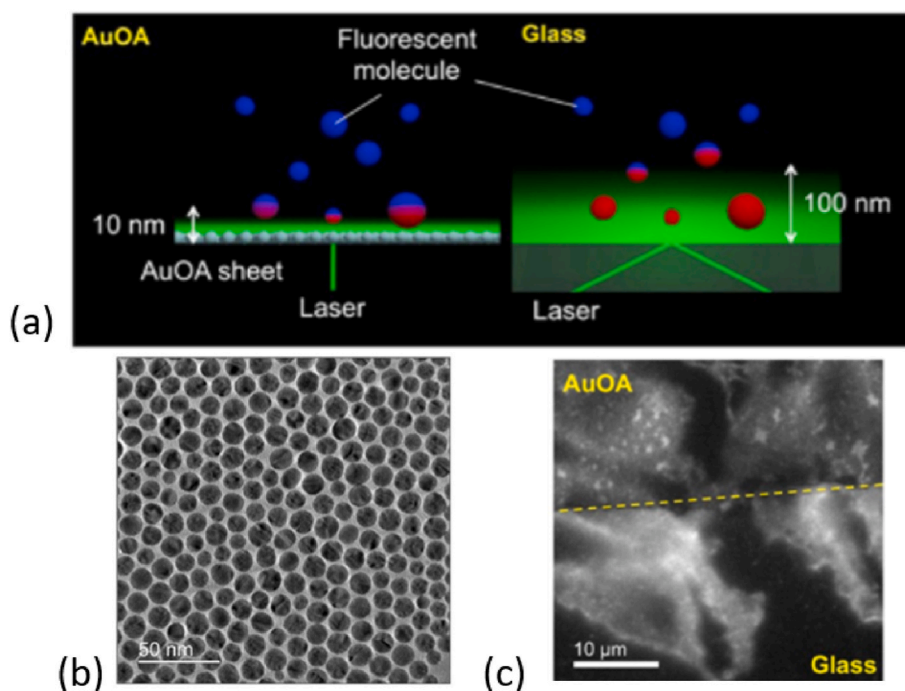

Fig. 14. a) Schematics of the probing depth upon the resonant excitation of the LSPs on Au NP sheet (AuOA) and evanescent field on glass surface with TIRF, b) TEM image of Au NP sheet and c) comparison of fluorescence images of labelled actin filaments in RBL-2H3 cells on AuOA and reference glass. Reproduced with permission from Ref. [159].

triggers fluorescence recovery. Characterization showed high quenching efficiency and significant fluorescence recovery, with an LOD of 0.68 nM. The study demonstrated the selective binding capability of the nanoplatform by comparing the fluorescence response to miRNA-21-1, miRNA-21–5p, and miRNA-141. Additionally, the platform showed good biocompatibility, low cytotoxicity, and effective intracellular uptake, selectively highlighting miRNA-21 in high-expression colorectal cancer cells while showing negligible fluorescence in low-expression and CD44-negative cell line, FHC.

6.2. Cell imaging with surface-attached nanostructures

A considerable amount of studies highlights the potential of PEF to provide significant improvements in the brightness, resolution, and sensitivity of fluorescence microscopy for more detailed and accurate visualization of cellular structures and processes. The 2D plasmonic grating substrate was produced using a UV-nanoimprint method and coated with Ag layer for fluorescence microscopy imaging of neuronal cells [157]. The plasmonic substrate allowed for diffraction-based excitation of PSP modes and was integrated into a dish. It substitutes the traditional cover glass with a silver-coated grating substrate for *in situ* imaging of neuronal cells by employing epi-illumination geometry. The neuronal cells were successfully cultured on the substrate for over two weeks and there were captured both epi-fluorescence and transmitted-light fluorescence images. By optimizing the setup for detailed visualization of neuronal cells and their dendrites there was reported up to a 10-fold increase in brightness and improved spatial resolution. In the second study, the plasmonic dish was integrally molded from cyclo-olefin polymers with a wavelength-scale periodic structure and coated with thin metal films [158]. The plasmonic dish was composed of Ti/Ag/Ti/SiO$_2$ layers and by using diffraction grating-coupled PSPs the study showed that the images of human embryonic kidney cells were 14–17 times brighter with the 10 × objective lens while they were 7-times brighter with 40 × than those obtained with traditional glass-bottomed dishes. The dish also allowed for culturing of neuronal cells for ten days, emphasizing its adaptability for various cell types and its practicality for large-scale bioimaging use.

Two-dimensional AuNP sheets supporting LSPs were applied for fluorescence microscopy – based studies of cells [159]. This technique leverages the tighter confined electromagnetic field of LSPs compared to PSPs to improve spatial resolution. Unlike complex scanning systems, this method allows for nanometer-scale visualization of cellular structures in real-time. Experiments conducted on rat basophilic leukemia (RBL-2H3) cells demonstrated substantial improvements in image quality and spatial resolution in the direction perpendicular to the surface (see Fig. 14), with notably increased overall fluorescence signal with respect to using regular TIRF microscopy. The fluorescence enhancement factor due to LSPR was determined to be up to 50. The reported findings were consistent with recent morphological studies of the actin cytoskeleton using super-resolved fluorescence microscopy and offered the advantage of fast non-scanning imaging technique. Besides Au NP sheets, also substrates with Au nanostar NP (AuNST) were tested for imaging of cells and they provided up to 19-fold fluorescence intensity enhancement within the NIR biological window, facilitating the use of low-quantum yield fluorophores for detailed cellular imaging [160]. The researchers utilized monolayers of AuNST with sizes of 47 ± 17 nm and 214 ± 90 nm, respectively attached to silanized glass slides. HeLa cells, which overexpresses Folate Receptor alpha (FRα), were labelled with antibodies conjugated with the NIR fluorophore Alexa Fluor 680. The labelled cells were then adsorbed onto AuNST arrays and imaged using a confocal microscope.

Besides dominantly used Au and Ag structures, thin Al layers were employed in deep-ultraviolet SPR for amplified fluorescence excitation and cell imaging [160]. ATR configuration in Kretschmann geometry was employed with 21 nm Al layer for imaging of stained MC3T3-E1 cells with fluorescence intensity enhanced three-fold with respect to

conventional methods, providing clearer and more detailed images of dye-labelled cells.

PEF found not only applications in monitoring intracellular biomolecules and imaging of stained cell structures, but also in investigating protein secretion dynamics. Macrophages, dendritic cells, and dendritic T-cell co-cultures were exposed to biochemical stimuli such as lipopolysaccharide, inflammasome activation, and *Mycobacterium tuberculosis* infection and secreted stress biomarkers were detected in a spatially resolved manner [161]. By mapping the spatial distribution of secreted proteins around single cells, differences in secretion patterns of TNF-a and IL-1b were observed. The used sandwich immunoassay relied on labels incorporating amplifying colloidal nanoparticles capped with fluorescence emitters (FluoroDOT). These plasmonic labels were 1.6 × 10^4 times brighter and provided nearly 30-times higher signal-to-noise ratio compared to conventional fluorescence labels. They allowed for high-resolution imaging of different secreted cytokines, both in single-plexed and multiplexed formats, revealing cellular heterogeneity in the secretion of multiple proteins simultaneously. The LODs for TNF-a, IL-6, and interferon-gamma (IFN-g) were 670 fg/mL, 8 fg/mL, and 3.17 pg/mL, respectively. However, this method is currently only applicable to adherent cells. Retaining non-adherent and loosely adherent cells on the plate is challenging, as they tend to detach during the process. Another limitation is that the current algorithm can only analyze isotropic secretions, which are uniform in all directions. However, some cells, like macrophages and neurons, exhibit unidirectional secretion patterns that are elongated and not captured by this method.

7. Applications in environmental monitoring

Environmental contamination imposes a significant threat to the human population and nature vulnerable to various pollutants. Their major part originates from human activities and enters into the environment through pathways like industrial effluents, biomedical waste, gas emissions, and agricultural chemicals. The further discussion centres around the advances of PEF-based sensors and biosensors for monitoring pollutants providing information on the analytical performance in comparison to limits set by the regulatory bodies. The below discussion also highlights the different sensing materials like polymers, 2D materials like graphene, mesoporous materials and metal-organic frameworks (MOFs) employed for the detection of pollutant by PEFs. An overview of targeted analytes is arranged along the lines of heavy metal ion pollution in water, detection of presides in water and soil, and the analysis of pharmaceutical residues in water and food-derived matrices.

7.1. Heavy metal ions

Industrial effluents, containing substances like dyes, surfactants, minerals, and toxic heavy metals, endanger aquatic life and ecosystems. Release of these effluents introduces harmful metals such as chromium, copper, lead, ion, manganese, cadmium, mercury, nickel, and zinc into water bodies that can leach e.g. to potable water sources. Regulatory bodies such as the World Health Organization (WHO), the Environmental Protection Agency (EPA), and the Food and Agriculture Organization (FAO) set concentration limits for these pollutants, considering exceeding these limits as hazardous for living organisms [162]. For instance, WHO's permissible limits for heavy metal ions in drinking water include 0.05 ppm for Arsenic (As-III/V), Lead (Pb-II), and 0.005 ppm for Cadmium (Cd-II), Chromium (Cr-VI/III), 0.001 ppm for Mercury (Hg), and 1.5 ppm for Copper (Cu-II). In comparison, the US EPA has established limits of 0.01 ppm, 0.015 ppm, 0.005 ppm, 0.05 ppm, 0.002 ppm, and 1.3 ppm, respectively, for the same pollutants [163]. As shown by further discussed examples and overview in Table 6, recent progress in mostly colloidal metallic nanoparticle – based system provides routes to detect these analytes with the required sensitivity.

Optical sensors, particularly fluorescence ones, have been proven as valuable analytical tools providing high specificity, low detection limits,

Table 6

Overview of PEF-based techniques developed for the analysis of heavy metal ions.

Target analyte	Analyte sensitive material and PEF structure	LOD/WHO limit	Upper range	Ref.
Pb^{2+}	PAN/Ag/SiO$_2$ nanofibrous mat with CPE solution	17 pM (0.003 ppb)/0.05 ppm	3.0 μM	[164]
Pb^{2+}	GQDs/AuNPs	16.7 nM (3.460 ppb)/0.05 ppm	4 μM	[168]
Pb^{2+}	HS-C/Au (1.4) UiO-66	8 ppt/0.05 ppm	10 ppb	[174]
Hg^{2+}	Aptamer-Ag@SiO$_2$ NPs	0.33 nM (0.066 ppb)/0.001 ppm	900 nM	[175]
Hg^{2+}	PCP conjugated with Au microplates	0.75 nM (0.150 ppb)/0.05 ppm	20 μM	[167]
Hg^{2+}	AgNP/rhodamine 6G thioamide	0.03 ppb/0.001 ppm	3 μM	[172]
Hg^{2+}	AuNC-modified paper substrate	1.2 nM (0.240 ppb)/0.001 ppm	1 μM	[176]
Hg^{2+}	Pyridoxal conjugated BSA-AuNCs	31.9 nM (6.39 ppb)/0.05 ppm	1.75 μM	[177]
Hg^{2+}	PVP-Au	100 nM (20.04 ppb)/0.05 ppm	60 μM	[166]
Hg^{2+}	Hexagonal mesoporous silica (HMS-Ag-R)	0.9 ppb/1 ppb	110 ppb	[178]
Hg^{2+}	Rhodamine derivatives grafted AuNS@Ag core-shell nanocubes (CSN)	0.94 ppb/1 ppb	1000 ppm	[179]
Hg^{2+}	HMS-Ag-R-2SH	2.1 ppb/1 ppb	10 ppm	[180]
Ag^+	PVP/MMI-AuNC	17 nM/0.1 ppm	50 μM	[171]
Fe^{3+}	FITC/Au$_1$Ag$_4$@SiO$_2$	20 nM/3 ppm	63 μM	[165]
Cu^{2+}	Peptide-AuNCs	52 nmol/L/1.5 ppm	4.2 μM	[181]
Pb^{2+}	CuNCs with PEI, His, GSH	0.615 μM (0.127 ppb)/0.05 ppm	800 μM	[182]
Cu^{2+}		0.107 μM, (6.799 ppb)/1.5 ppm		
Cd^{2+}		0.650 μM, (20.04 ppb)/0.005 ppm		
Co^{2+}		0.322 μM (18.95 ppb)/0.01 ppm		
Ni^{2+}		0.265 μM (15.55 ppb)/0.07 ppm		
Zn^{2+}		0.827 μM (54.06 ppb)/5 ppm		
Cd^{2+}	AuNCs@NCDs	0.15 μmol/L, (18.04 ppb)/0.005 ppm	75 μM	[173]
Pb^{2+}		0.20 μmol/L, (41.44 ppb)/0.05 ppm	75 μM	
Hg^{2+}		0.09 μmol/L (10.11 ppb)/0.05 ppm	45 μM	
Cu^{2+}	Ag nanocube@SiO$_2$@PMOs	0.3 μM (19.063 ppb)/1.5 ppm	5 μM	[169]

rapid response, and simplicity for the analysis of heavy metals. A polyacrylonitrile (PAN)/noble metal/SiO$_2$ nanofibrous mat mixed with conjugated polyelectrolytes (CPE) was developed as a photonic crystal-enhanced fluorescence substrate [164]. As illustrated in Fig. 15a, the sensor utilized poly-(*p*-phenylene ethynylene) with hydrophilic sulfonate groups quenched by heavy metal ions through metal ions-induced aggregation. The sensor, especially effective for Pb^{2+} rather than for other heavy metal ions (see Fig. 15b), achieved an LOD of 17 pM. The same group designed a PEF sensor using fluorescence isothiocyanate (FITC)/Au1Ag4@SiO$_2$ for Fe^{3+} detection, reaching a 20 nM LOD [165]. Embedding fluorescent materials with plasmonic materials enhanced fluorescence intensity in both studies.

In another approach, heavy metal ions were detected utilizing colloidal polyvinyl pyrrolidone (PVP) capped AuNPs. These fluorescent PVP-AuNPs exhibited a selective interaction with Hg^{2+} ions, in comparison to other metal ions. By monitoring the Hg^{2+}-induced quenching PVP fluorescence signal, LOD for Hg^{2+} was determined to be 100 nM [166]. The same research group also developed a sensor array using three different Cu nanoclusters combined with polyethyleneimine, histidine, and glutathione to detect 12 metal ions (Pb^{2+}, Fe^{3+}, Cu^{2+}, Cd^{2+}, Cr^{3+}, Co^{2+}, Ni^{2+}, Zn^{2+}, Ag^+, Fe^{2+}, Hg^{2+}, and Al^{3+}). The corresponding LODs for these ions are provided in the linked Table 6. Water-soluble photosynthetic antenna Peridinin-chlorophyll-protein complexes were reported for the analysis of Hg^{2+} with the use of Au micro-plates [167]. This approach relied on oxidative-reductive reactions and specific binding interactions with Hg^{2+}. The sensor exhibited a gradual increase in the intensity of the characteristic fluorescence peak at a wavelength of 673 nm with rising concentrations of Hg^{2+}. The obtained relationship displayed a linear detection range up to a concentration of 42 μM, with an LOD of 0.75 nM. A recent study introduced a sensor for detecting Pb^{2+} ions using graphene quantum dots (GQDs) and AuNP quenching that was modulated by selective interaction with DNAzyme stands [168]. The sensor utilized a colloidal solution of complexed GQDs and AuNPs with complementary DNA strands. The device demonstrated a detection range of 50 nM to 4 μM for Pb^{2+} ions, with an LOD of 16.7 nM. Other researchers have introduced periodic mesoporous organosilicas (PMOS) designed specifically for detecting Cu^{2+} ions. This composite features a multilayer core-shell structure comprising colloidal Ag-nanocubes caped with PMO [169]. Its design involves the synthesis of Ag nanocubes, deposition of a silica spacer shell, and construction of

outer periodic mesoporous organosilicas. Upon interaction with Cu^{2+} ions, noticeable changes in fluorescence spectrum occur due to ring-opening mechanisms triggered by complexation inside the bis (rhodamine Schiff-base derivative) groups allowing detection of Cu^{2+} with LOD of 0.3 μM. Other investigations have reported similar studies with the utilization of Au$_{25}$-absorbed Ag@SiO$_2$ core-shell nanoparticles for the detection of Cu^{2+} ions [170].

Moreover, a fluorescence sensor array employing a single probe was used to distinguish heavy metal ion fingerprints. In this work, HAuCl$_4$ was chemically reduced with 2-mercapto-1-methylimidazole (MMI) and polyvinylpyrrolidone, producing fluorescent gold nanoclusters (AuNCs). The fluorescence emission of PVP/MMI-AuNC was pH-dependent, shifting from yellow (λ_{max} = 512 nm) to red (λ_{max} = 700 nm) spectral range at pH 12.0 and 6.0, respectively. When exposed to metal ions, PVP/MMI-AuNC exhibited distinct signals at wavelengths of 512 nm and 700 nm. This single probe successfully identified and differentiated seven heavy metal ions (Ag^+, Fe^{3+}, Fe^{2+}, Mn^{2+}, Sn^{2+}, Pb^{2+}, and Hg^{2+}), detecting concentrations as low as 17 nM (Ag^+), below the EPA's drinking water limit [171]. There are several other approaches utilized to prepare the PEF-based sensor to detect the heavy metal ions below the acceptable ranges. A combined colorimetric and fluorescence sensor concept based on rhodamine 6G thioamide was utilized [172], where the fluorescence signal was enhanced by AgNPs. The sensor showed improved Hg^{2+} LOD of 0.030 ppb (with silver nanoparticles) compared to 49 ppb (only with rhodamine 6G thioamide). A multichannel optical fluorescence sensor utilizing microtiter well plates with AuNP clusters and fluorescence probes including colloidal N-doped carbon dots was developed for heavy metal analysis [173]. Metal ions were detected in both tap water and soil extracts with the LOD for Cd^{2+}, Pb^{2+}, and Hg^{2+} determined to be 0.15, 0.20, and 0.09 μM, respectively. The MOF NH$_2$-UiO66 was functionalized with carbon dots and AuNPs for the detection of Pb^{2+} (Fig. 16a). A FRET mechanism was observed between the fluorescent HS-C layer and AuNPs on the UiO-66 surface within HS-C/Au/(x)/UiO-66 particles (Fig. 16b) enabling reching a LOD of 0.1 ppb for Pb^{2+} [174].

7.2. Pesticides

Pesticides, while effective against agricultural pests, heavily pollute the environment and can lead to contamination of water, soil, air, and
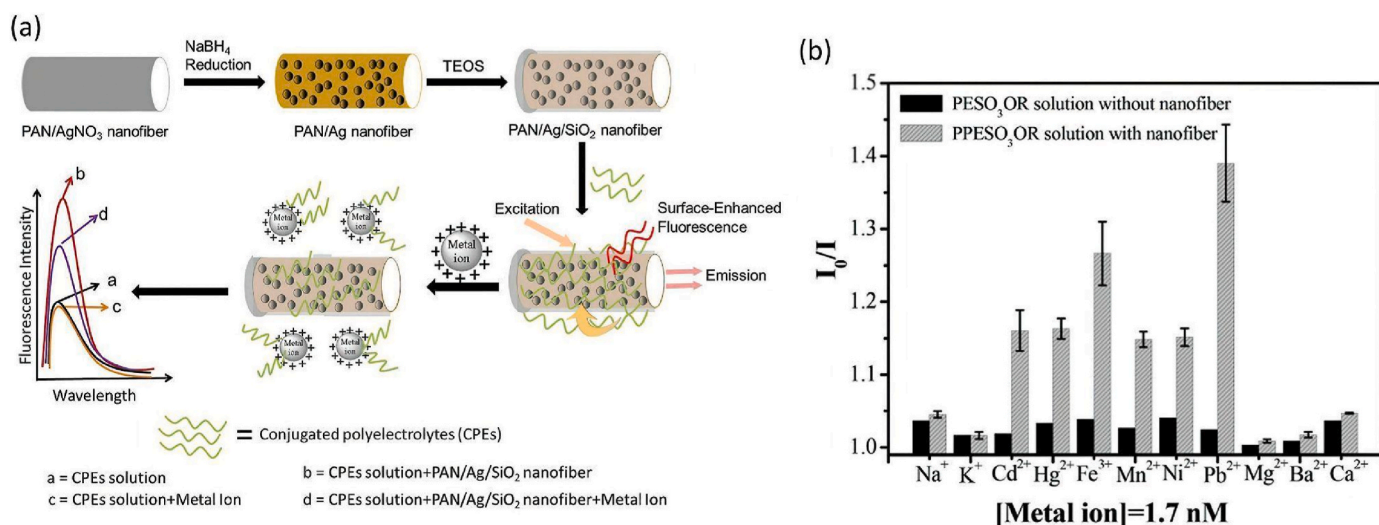
Fig. 15. a) A diagram depicting the fabrication process of PAN/Ag/SiO$_2$ nanofibers and the detection of metal ions through enhanced fluorescence and subsequent amplified fluorescence quenching, b) fluorescence graph with and without nanofiber. Reproduced from Ref. [164] with permission from the Royal Society of Chemistry.
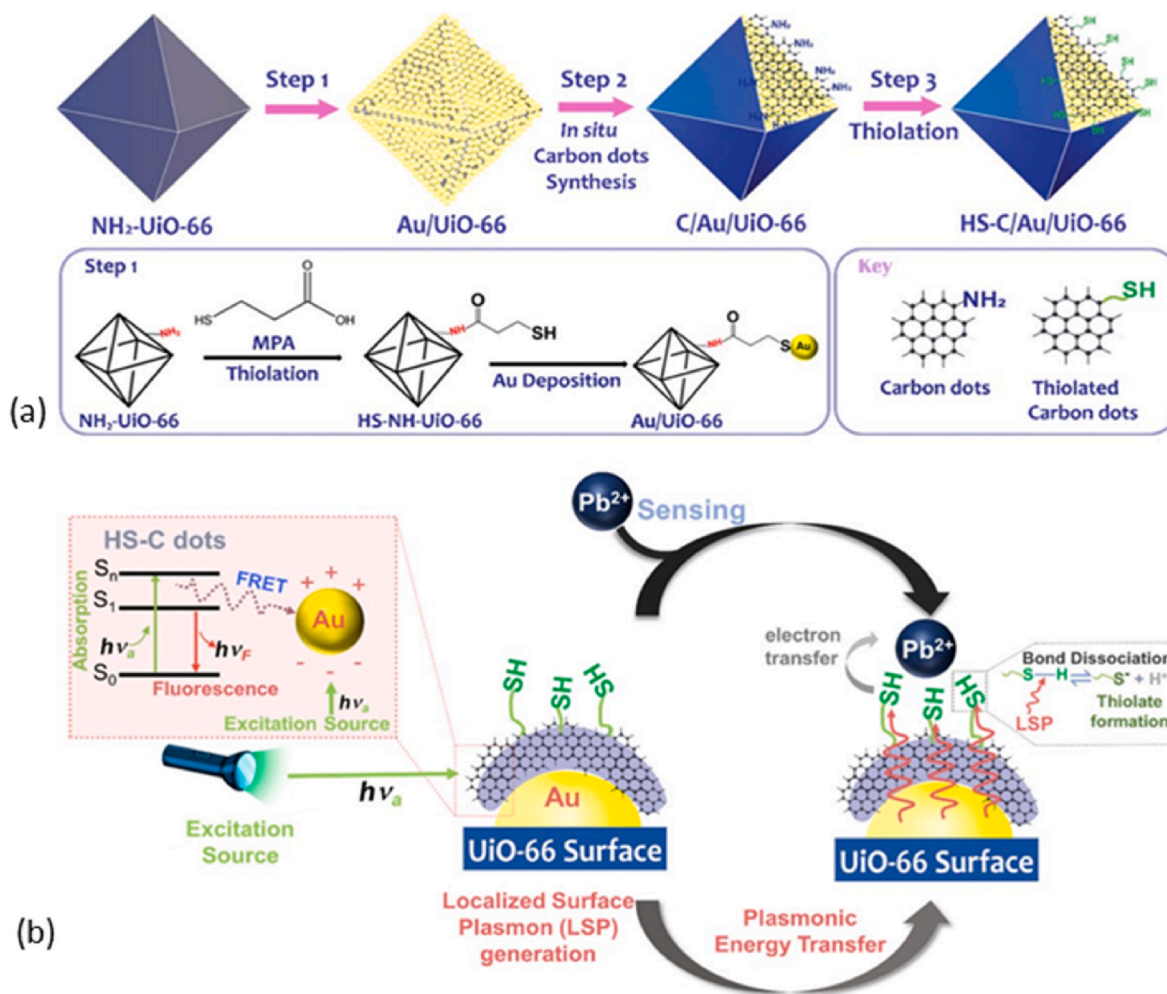

Fig. 16. a) Diagram outlining the creation process of HS-C/Au(x)/UiO-66, involving thiolation followed by preformed AuNP deposition on UiO-66 crystals in the first step. In step 2, *in situ* carbon dot synthesis takes place, followed by thiolation in the final step, b) FRET process that occurs between the fluorescent HS-C Layer and the AuNPs on the UiO-66 surface within HS-C/Au(x)/UiO-66 particles. Reproduced from Ref. [174] with permission from American Chemical Society.

Table 7

Overview of PEF sensors and biosensors targeting pesticides.

Target analyte	Plasmonic structure	LOD	Upper range	Ref.
Glyphosate	GSH-AuNC/ZIF8	0.28 nM	100 nM	[190]
2-aminoanthracine	AgBO/SiO$_2$	1 nM	800 nM	[191]
Paraquate	AuNC/β-CD/GSH	1.2 ng/mL	350 ng/mL	[192]
Carbendazim	AuNP/Rhodamine B	2.33 nM	800 nM	[193]
Thiram	AuNP/QD	7 nM	2 μM	[194]
Acetamiprid	AuNPs/DNA	1.67 pg/mL	150 ng/mL	[195]
Organophosphorus pesticides		0.17 fg/mL		
Organophosphorus pesticide	RB-Ag/Au	0.0018 ng/mL	0.28 ng/mL	[188]
Parathion-methyl	TMB2$^+$-mediated AuNR	2.42 ng/ml	5.00 μg/mL	[196]
Fenitrothion		0.95 ng/ml		
Fenthion		6.52 ng/ml		
Acephate	AuNC@ZIF-8	0.4 ng/mL	100 μg/mL	[189]
Paraoxan	AgNPs/SiO$_2$/OPH-pyranine derivative	1 ppb	100 ng/mL	[197]
Diazionon	AuNP/imidazole	53.3 ppb,	1 ppm	[198]
Iprobenfos		53.6 ppb		
Edifenphos		27.9 ppb		
Ethion	Ag–AuNP bimetallic	228 ppm	66.2 μM	[199]
Parathion		231 ppm		
Malathion		1189 ppm		
Fenthion		1835 ppm		
Dimethoate	AuNP/RB	4 ppb	1.0 ppm	[200]
Mancozeb	Ag nanoprism	5 ng/mL	100 ng/mL	[187]
Parathion	Au/Pt nanozyme	9.88 ng/kg	150 μg/kg	[201]
Triazophos		3.91 ng/kg		
Chlorpyrifos		1.47 ng/kg		
Dichlorvos	AuNP/IDA	0.03 mg/kg	4 mg/kg	[202]
Trichlorfon		9 μg/kg		
Paraoxon		7 μg/kg		

food sources. Pesticides residues harm non-target species including the human population, raising concerns about the impact to ecosystems and the safety of food and water resources [183]. Pesticides in water sources can lead to severe health issues in humans, including respiratory problems and cancer, making regular monitoring essential to ensure safe drinking water [184]. Environmental ecosystems are also at risk, as pesticides disrupt aquatic life and damage biodiversity, impacting their delicate balance. Furthermore, contaminated water used in agriculture jeopardizes crop yields, leading to economic losses for farmers [185]. By detecting pesticides in water, timely interventions can be implemented to safeguard public health, protect ecosystems, and sustain agriculture, highlighting the critical importance of monitoring and addressing pesticide contamination in water sources. In order to monitor the presence of these compounds, established analytical techniques like gas chromatography and liquid chromatography with mass spectrometry represent the currently used gold standard methods [186]. However, they typically rely on bulky instruments that need to be deployed in specialized laboratories and require operation with highly trained personnel. In order to simplify the analysis and allow for more frequent on-site tests without the need of transporting the analyzed samples to central laboratories, fluorescent sensors, and biosensors have emerged as a cost-effective, efficient, and rapid solution for direct pesticide

detection. PEF-based sensors and biosensors offer a route to enhance sensitivity for detecting pesticides in order to fulfil limits stipulated by regulatory bodies. For instance, the U.S. Environmental Protection Agency set permissible limits for pesticides such as glyphosate at 0.7 ppm and paraquat at 0.03 mg/L. In the below sections, the selection of work reporting on PEF-based methodologies pursued for the detection of compounds relevant to environmental monitoring applications is presented with an overview of analytes included in Table 7.

Mancozeb is a dithiocarbamate non-systemic agricultural fungicide used in vegetables and fruits (see Table 8). Recently, there was reported a dual fluorimetric and colorimetric sensor that employs fluorescein as a reporter and Ag nanoprisms (Ag-NPRs) as fluorescence intensity enhancer. The detection mechanism is based on the interaction between Ag-NPRs and mancozeb that is mediated by thiosulfate ions (S$_2$O$_3$$^{2-}$) and affects the stacking of Ag-NPRs. The addition of S$_2$O$_3$$^{2-}$ decreases the fluorescence enhancement effect of Ag-NPRs and detunes the LSPR wavelength, but mancozeb restores both fluorescence intensity and the SPR peak position of Ag-NPRs. The detection limits of the fluorimetric and colorimetric sensor was of 2.0 and 3.0 ng/mL, respectively, with a concentration range of 0.005–0.1 μg/mL [187].

Organophophorous (OP) chemicals dominate pesticides and germicides used in agriculture. Even at modest doses, OP substances are toxic

Table 8

Comparison of PEF sensors and biosensors developed for pharmaceutical residues.

Target analyte	Plasmonic nanostructure	LOD	Upper range	Ref.
Ciprofloxacin	AgNP	90 pg/mL	1.0 μg/mL	[209]
Enrofloxacin		5 pg/mL	160 pg/mL	
Lomefloxacin		6 pg/mL	0.8 μg/mL	
Cephalexin	gCDc/AuNCs/ZIF-8	0.04 ng/mL	6 ng/mL	[208]
Ciprofloxacin	Al^{3+} and AuNC templated with glutathione	1.4 nM	120 μM	[210]
Danofloxacin	AuNP	7.5 μM	50 μM	[211]
Ciprofloxacin		7.5 μM	96 μM	
Norfloxacin		10 μM	133 μM	
Tetracycline	AgNP/carbon dot	0.6 ng/mL	3 μg/mL	[206]
Tetracycline	AgNP/CdTe QD	16.2 nM	0.4 mM	[228]
Tetracycline	AgNP	4.8 nM	10 μM	[207]
Kanamycin	bovine serum albumin stabilized AuNCs (BSA-AuNCs)	32 pM	7.0 nM	[212]
Kanamycin	Aptasensor based on Exo III and AuNPs	321 pM	100 nM	[213]

to humans. The construction of a fluorescent instrument with high selectivity and sensitivity was accomplished using straightforward techniques. Ag/Au bimetallic NPs modified with Rhodamine B (RB) were utilized. The fluorescence of RB-Ag/AuNPs was diminished until they were exposed to OP pesticides. Due to the stronger cooperation between Ag/AuNPs and OPs than with RB, RB fluorescence recovers as the molecule departs Ag/AuNPs. The LOD for OPs in fruit and water samples was od 1.8 pg/mL [188]. MOF are frequently combined with AuNCs for PEF sensors. Integration of MOFs with AuNC was, for instance, employed in the aggregation-induced emission detection principle of OPs based on quenching of enzymolysis by acetylcholinesterase and choline oxidase. This approach was reported for on-site quantitative OP detection with an LOD of 0.4 g/L [189].

7.3. Pharmaceutical residues

The widespread use of antimicrobial substances like antibiotics leads to the infiltration of aquatic ecosystems. The introduction of antibiotic medications and pharmaceutical goods into water ecosystems can occur through multiple pathways. As individuals consume antibiotics or other pharmacological chemicals, these compounds pass through metabolic processes resulting in the excretion of both unaltered and partially modified molecules through urine and faeces. Therefore, pharmaceutical chemicals have the potential to enter to wastewater systems via sewage treatment plants [203]. In addition, the act of direct disposing of pharmaceutical compounds into wastewater further strengthen this leaching into the environment where these substances can interfere with the behaviour, growth, and reproductive processes of aquatic species [204]. Furthermore, antibiotics, crucial for managing infections, contribute to bacterial resistance, posing unpredictable threats to human health [205]. As traditional wastewater treatment methods struggle to degrade antibiotics effectively, exacerbating environmental issues, the monitoring of antibiotics in water sources is critical. Selected examples of PEF sensors developed for precise identification and evaluation of antibiotics are summarize in Table 8 with more detail discussion give further in this section.

Ag/carbon dot (Ag/CD) nanoparticles were devised for detecting tetracycline (TC) that has an intrinsic fluorescence. Its interaction with LSPR on AgNPs provided the PEF and offering a sensor with the LOD of 0.6 ng/mL (1.2 nM) and a linear detection range of 0.025–3 μg/mL in water [206]. Another sensor for TC developed by AgNP-enhanced fluorescence when incorporated to natural halloysite nanotubes. Besides the PEF-based detection, the modified Ag nanoparticles promote electron-hole separation, boosting the platform's catalytic activity and aiding in the degradation of TC residues. This platform achieved LOD of 4.8 nM for TC with a detection range spanning to 10 μM in aqueous solution and detection in milk was also demonstrated [207].

Antibiotics in milk were also detected using a ratiometric fluorescent probe that utilizes the simultaneous integration of AuNCs and green emitting carbon dots (gCDs) into ZIF-8 for the purpose of analyzing cephalexin (CFX). The sensor exhibited a dual emission at wavelengths of 520 and 630 nm when subjected to an excitation wavelength of 400 nm. The fluorescence emission of AuNCs at a wavelength of 630 nm is specifically suppressed by the presence of CFX, while the fluorescence emission of graphene quantum dots (gCDs) at a wavelength of 520 nm remains relatively unaffected. The fluorescence signal ratio (F520/F630) of the composite (gCDc/AuNCs @ ZIF-8) exhibits a linear relationship with the concentration of CFX within the range of 0.1–6 ng/mL with a LOD of 0.04 ng/mL, which falls below the maximum residues limit of 100 ng/mL established by the U.S. Food and Drug Administration (FDA) [208].

8. Single-molecule analysis

Fluorescence measurements of optical signals originating from individual molecules capitalize on the already established optical instrumentations and availability of fluorophores with high quantum yield η. In conjunction with spatially confined optical probing that was utilized by small metallic cavities referred as to zero-mode waveguides (ZMW), such capability paved the way to important technologies for sequencing nucleic acid-based molecules. It serves for the monitoring of the reaction of ssDNA chain fragments with individual fluorophore-labelled nucleotides diffusing into the cavity [214]. The spatially confined optical probing allows to efficiently block background from the nucleotides present in bulk solution and provides means to follow in real time the assembling of complementary strands by one-by-one incorporation of (fluorophore-tagged) nucleotides.

ZMW are typically prepared in the form of nanoholes with a diameter D ranging from 50 to 200 nm in a 100 nm thick Al layer to restrict the optical probing to aL -zL volume, which is substantially below fL volumes achievable by regular diffraction-limited focal volume of optical microscopes. They are designed for operating in broad wavelength range and their plasmonic properties are not exploited. However, by engineering the geometry of the nanoapertures (circular, rectangular, elliptical) and using other types of metals such as Au or Ag, plasmonic manipulation with fluorophore emitters can be introduced. In particular, the PEF in such ZMW cavities was proposed for improved time resolution enabling measurements of fast biomolecular dynamics [215].
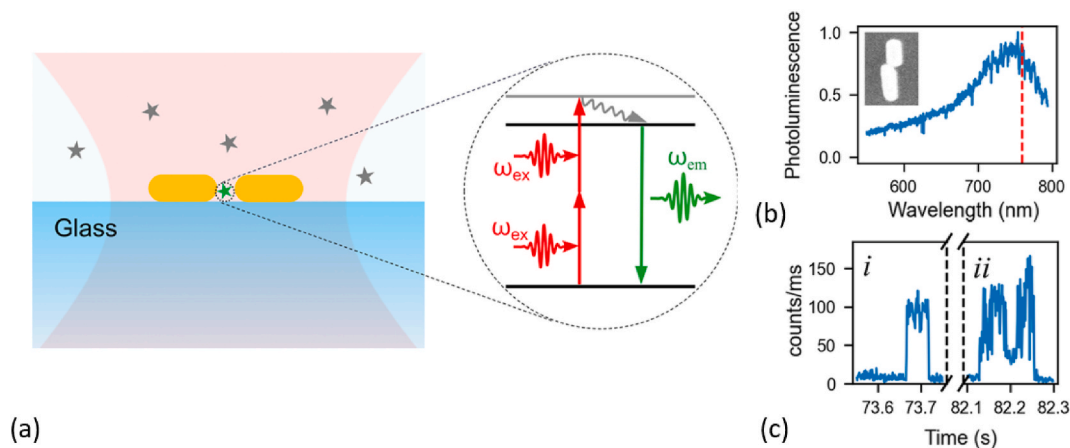

Fig. 17. a) Schematics of AuNR dimer plasmonic nanoantenna for amplification of two photon - excited fluorescence from a fluorophore diffusing through plasmonic hotspot with an example of b) LSPR spectrum measured with one photon luminescence and c) intensity traces with two-photon excited fluorescence bursts. Adapted and reproduced with permission from Ref. [71].

Moreover, a possible combination of nanopore-based sequencing based on electronic readout with optical detection was explored by integrating nanopore structures with plasmonic metallic apertures [216]. Besides PEF, other spectroscopy tools such as surface-enhanced Raman spectroscopy were proposed [217] and the possibility of exploiting phenomena including local molecular trapping and plasmonic heating was discussed [218].

In another route, surface-attached lithographically prepared nanopores and plasmonic nanoantennas were proposed for the monitoring of fluorophore-tagged molecules based on fluorescence correlation spectroscopy (FCS) [219]. This approach allowed for plasmonic enhancement of recorded fluorescence intensity and it strongly decreased probing volume in comparison to conventional FCS. Then, monitoring of diffusing through the narrowed probed volume is possible for individual molecules present at high (up to μM) concentrations [220] that are close to natural conditions in biological systems. This research direction is expected to contribute to studying of new phenomena occurring at single molecule level that stay hidden from conventional techniques relying on the probing of molecular ensembles. Similar functionality was reported also with chemically synthesized plasmonic nanoantennas enabling PEF recording of diffusion and surface attachment of individual dye molecules [221] and this work paved the way for more recent results demonstrating two-photon excitation and detection of single molecules [71]. As Fig. 17 shows, AuNR dimers were assembled and used for the confocal microscope-based probing of the formed plasmonic hotspot used for the monitoring of molecules passing through upon the excitation with pulsed fs laser beam. These events manifested themselves as a series of fluorescence intensity bursts, which were amplified by a factor of up to 5×10^7 with respect to those present in the bulk solution (see Table 1).

Besides FCS-related works, a new generation of PEF biosensors capable of monitoring individual affinity binding events is emerging based on DNA origami structures (which can be designed to self-assemble in controlled 2D and 3D geometries, see Fig. 6) [222]. Constructs with predefined functionalization locations can be used to precisely attach individual BREs to plasmonic hotspots at distances from metallic nanoparticles that allow avoiding quenching and ensure maximum enhancement [90,223]. Furthermore, when driving the fluorophores at excitation rate γ_e close to saturation regime, photon count rates γ_r larger than 1 million photons/s/molecule were reported, allowing to maximize time resolution and binning times at 10 μs range [224,225]. Functionalized DNA origami plasmonic nanoantennas were demonstrated for single fluorophore measurements with $EF > 400$ [223] and were also implemented for the detection of biomolecules. It was demonstrated to resolve affinity binding of individual ssDNA and ssRNA sequences specific for Zika virus in biologically relevant sample by using direct MB-based assay [68,226]. In addition, the detection of single antibody recognizing digoxigenin in conjunction with a nanoswitch placed in the hotspots was reported [227]. Upon binding of the anti-digoxigenin, the nanoswitch opens up and modulates a distance from a quencher competing with PEF.

9. Summary and outlook

Since initial investigations of the coupling between fluorescent emitters and surface plasmon resonances on metallic nanostructure demonstrated the ability to efficiently amplify fluorescence signal, we witness flourishing amounts of its applications in analytical technologies for the analysis of chemical and biological compounds. Within the last decade, the field of plasmon-enhanced fluorescence – PEF – benefited from improved preparation routes for metallic nanostructures with well-controlled plasmonic characteristics by means of lithography as well as chemical synthesis. Besides the fabrication precision, efforts were devoted to the development of protocols that allow for cost-efficient preparation of the structures suitable for disposable use. Even without complex lithography preparation routes extraordinarily high fluorescence enhancement factors $EF > 10^3$ were reported, which is essential for the utilization in highly sensitive practical analytical tests. Moreover, non-linear optical techniques such as those relying on two-photon excitation can benefit further improved enhancement factors reaching the level of $EF > 10^7$.

In conjunction with the advancements in biointerfaces and assay formats powered by other (non-optical) amplification means including enzymatic rolling circle amplification or catalytic hairpin assembly, PEF paved the way for ultrasensitive analysis of nucleic acid as well as protein–based analytes. These assays were implemented by the use of established laboratory equipment such as fluorescence microarray or microtiter plate readers and allowed reaching LODs below fM concentrations for target compounds present in complex biological fluids. This performance is comparable to the gold standard tools including digital polymerase chain reaction or digital ELISA techniques used for high sensitivity analysis of nucleic acids and proteins, respectively. In particular in the field of biomarkers analysis and detection of harmful species relevant to medical diagnostics, the sensitivity in conjunction with the simplified detection format holds the potential to establish PEF method in the field of expanding the medical molecular diagnostics market. Environmental monitoring represents another field that was particularly addressed by PEF sensors and biosensors. These efforts aim to deliver simplified yet sufficiently sensitive detection schemes in order to allow for on-site analysis that is currently not possible to realize with standardly used mass spectrometry – based techniques.

Moreover, PEF plays an important role in emerging research branch devoted to single-molecule detection and single-molecule interaction analysis. We witness its implementations in the context of fluorescence correlation spectroscopy-based monitoring of biomolecular interactions and in the direction of cell imaging and intracellular biomolecule detection supporting life science research. Most commonly, studies in single molecule detection that are powered by PEF rely on dedicated instruments or high-end fluorescence microscopes. However, efforts to expand the availability of such experiments by using more affordable optics, where the limited performance of used components is compensated by the PEF – based amplification, have been documented.

In a nutshell, over the last decade the field of PEF rapidly developed in terms of precise construction of metallic nanostructures with apparent advances achieved by using chemically synthesized metallic nanostructures as facile building blocks. Based on these materials, numerous studies reported fluorescence signal enhancement factors EF exceeding the magnitude of 10^3 that before were accessible only with nanostructures prepared by advanced lithography techniques. These materials found greatly expanding range of applications and served on solid substrates (e.g. on chips for immunoassays and assays for sensitive detection of nucleic acids), but also more frequently are being exploited in solution-based detection strategies. Besides already recognized application fields dealing with ultrasensitive and portable detection of chemical and biological species, also new areas associated with single molecule detection and applications in life science studies with e.g. cell imaging have emerged and can be expected to take momentum in future research and application directions.

CRediT authorship contribution statement

Dario Cattozzo Mor: Writing – review & editing, Writing – original draft. **Gizem Aktug:** Writing – review & editing, Writing – original draft. **Katharina Schmidt:** Writing – review & editing, Writing – original draft. **Prasanth Asokan:** Writing – review & editing, Writing – original draft. **Naoto Asai:** Writing – review & editing, Writing – original draft. **Chun-Jen Huang:** Writing – review & editing, Funding acquisition. **Jakub Dostalek:** Writing – review & editing, Writing – original draft, Funding acquisition, Conceptualization.

Declaration of competing interest

The authors declare that they have no known competing financial interests or personal relationships that could have appeared to influence the work reported in this paper.

Acknowledgments

Appendix A. Supplementary data

Supplementary data to this article can be found online at https://doi.org/10.1016/j.trac.2024.118060.

Data availability

The raw data that support this study are openly available in Zenodo (https://doi.org/10.5281/zenodo.12516384).

References

[1] H. Altug, et al., Advances and applications of nanophotonic biosensors, Nat. Nanotechnol. 17 (1) (2022) 5–16.

[2] B. Liedberg, C. Nylander, I. Lunström, Surface plasmon resonance for gas detection and biosensing, Sens. Actuator. 4 (1983) 299–304.

[3] J. Homola, Surface plasmon resonance sensors for detection of chemical and biological species, Chem. Rev. 108 (2) (2008) 462–493.

[4] L. Huang, et al., Hierarchical plasmonic-fluorescent labels for highly sensitive lateral flow immunoassay with flexible dual-modal switching, ACS Appl. Mater. & Interfac. 12 (52) (2020) 58149–58160.

[5] J. Yang, et al., Recent advances in colorimetric sensors based on gold nanoparticles for pathogen detection, Biosens. 13 (2023), https://doi.org/10.3390/bios13010029.

[6] J. Langer, et al., Present and future of surface-enhanced Raman scattering, ACS Nano 14 (1) (2020) 28–117.

[7] R. Adato, S. Aksu, H. Altug, Engineering mid-infrared nanoantennas for surface enhanced infrared absorption spectroscopy, Mater. Today 18 (8) (2015) 436–446.

[8] T. Liebermann, W. Knoll, Surface-plasmon field-enhanced fluorescence spectroscopy, Colloids Surf. A Physicochem. Eng. Asp. 171 (1) (2000) 115–130.

[9] J.R. Lakowicz, et al., Directional surface plasmon-coupled emission: a new method for high sensitivity detection, Biochem. Biophys. Res. Commun. 307 (3) (2003) 435–439.

[10] O.F. Silvestre, A. Rao, L.M. Liz-Marzán, Self-assembled colloidal gold nanoparticles as substrates for plasmon enhanced fluorescence, Euro. J. Mater. 3 (1) (2023) 1–29.

[11] M. Bauch, et al., Plasmon-enhanced fluorescence biosensors: a review, Plasmonics 9 (4) (2014) 781–799.

[12] J.-F. Li, C.-Y. Li, R.F. Aroca, Plasmon-enhanced fluorescence spectroscopy, Chem. Soc. Rev. 46 (13) (2017) 3962–3979.

[13] J. Dong, et al., Recent progress on plasmon-enhanced fluorescence 4 (4) (2015) 472–490.

[14] D. Semeniak, et al., Plasmonic fluorescence enhancement in diagnostics for clinical tests at point-of-care: a review of recent technologies, Adv. Mater. 35 (34) (2023) 2107986.

[15] Y. Jeong, et al., Metal enhanced fluorescence (MEF) for biosensors: general approaches and a review of recent developments, Biosens. Bioelectron. 111 (2018) 102–116.

[16] S.M. Fothergill, C. Joyce, F. Xie, Metal enhanced fluorescence biosensing: from ultra-violet towards second near-infrared window, Nanoscale 10 (45) (2018) 20914–20929.

[17] M. Jahn, et al., Plasmonic nanostructures for surface enhanced spectroscopic methods, Analyst 141 (3) (2016) 756–793.

[18] E. Prodan, et al., A hybridization model for the plasmon response of complex nanostructures, Sci 302 (5644) (2003) 419–422.

[19] J.J. Mock, et al., Distance-dependent plasmon resonant coupling between a gold nanoparticle and gold film, Nano Lett. 8 (8) (2008) 2245–2252.

[20] E. Hao, G.C. Schatz, Electromagnetic fields around silver nanoparticles and dimers, J. Chem. Phys. 120 (1) (2004) 357–366.

[21] D. Dey, G.C. Schatz, Plasmonic surface lattice resonances in nanoparticle arrays, MRS Bull. 49 (5) (2024) 421–430.

[22] G. Vecchi, V. Giannini, J. Gómez Rivas, Surface modes in plasmonic crystals induced by diffractive coupling of nanoantennas, Phys. Rev. B 80 (20) (2009).

[23] D. Kotlarek, et al., Actuated plasmonic nanohole arrays for sensing and optical spectroscopy applications, Nanoscale 12 (17) (2020) 9756–9768.

[24] G.W. Ford, W.H. Weber, Electromagnetic interactions of molecules with metal surfaces, Phys. Rep. 113 (4) (1984) 195–287.

[25] N. Gisbert Quilis, et al., Actively tunable collective localized surface plasmons by responsive hydrogel membrane, Adv. Opt. Mater. 7 (15) (2019) 1900342.

[26] V. Flauraud, et al., In-plane plasmonic antenna arrays with surface nanogaps for giant fluorescence enhancement, Nano Lett. 17 (3) (2017) 1703–1710.

[27] S. Tiwari, et al., Achieving high temporal resolution in single-molecule fluorescence techniques using plasmonic nanoantennas, Adv. Opt. Mater. 11 (13) (2023).

[28] N. Gisbert Quilis, et al., Tunable laser interference lithography preparation of plasmonic nanoparticle arrays tailored for SERS, Nanoscale 10 (21) (2018) 10268–10276.

[29] M. Vala, J. Homola, Flexible method based on four-beam interference lithography for fabrication of large areas of perfectly periodic plasmonic arrays, Opt. Express 22 (15) (2014) 18778.

[30] S. Fossati, et al., Multiresonant plasmonic nanostructure for ultrasensitive fluorescence biosensing, Nanophoton. 9 (11) (2020) 3673–3685.

[31] J. Chen, et al., Gold nanohole arrays for biochemical sensing fabricated by soft UV nanoimprint lithography, Microelectron. Eng. 86 (4) (2009) 632–635.

[32] J.-F. Masson, M.-P. Murray-Méthot, L.S. Live, Nanohole arrays in chemical analysis: manufacturing methods and applications, Analyst 135 (7) (2010) 1483.

[33] M. Cottat, et al., Soft UV nanoimprint lithography-designed highly sensitive substrates for SERS detection, Nanoscale Res. Lett. 9 (1) (2014) 623.

[34] N. Vogel, et al., Advances in colloidal assembly: the design of structure and hierarchy in two and three dimensions, Chem. Rev. 115 (12) (2015) 6265–6311.

[35] C. Hanske, et al., Solvent-assisted self-assembly of gold nanorods into hierarchically organized plasmonic mesostructures, ACS Appl. Mater. & Interfac. 11 (12) (2019) 11763–11771.

[36] Z. Mei, L. Tang, Surface-plasmon-coupled fluorescence enhancement based on ordered gold nanorod array biochip for ultrasensitive DNA analysis, Anal. Chem. 89 (1) (2017) 633–639.

[37] N. Liu, T. Liedl, DNA-assembled advanced plasmonic architectures, Chem. Rev. 118 (6) (2018) 3032–3053.

[38] R. Schreiber, et al., Hierarchical assembly of metal nanoparticles, quantum dots and organic dyes using DNA origami scaffolds, Nat. Nanotechnol. 9 (1) (2014) 74–78.

[39] A. Puchkova, et al., DNA origami nanoantennas with over 5000-fold fluorescence enhancement and single-molecule detection at 25 μM, Nano Lett. 15 (12) (2015) 8354–8359.

[40] A. Kuzyk, et al., DNA-based self-assembly of chiral plasmonic nanostructures with tailored optical response, Nature 483 (7389) (2012) 311–314.

[41] A. Kuzyk, et al., Reconfigurable 3D plasmonic metamolecules, Nat. Mater. 13 (9) (2014) 862–866.

[42] P. Anger, P. Bharadwaj, L. Novotny, Enhancement and quenching of single-molecule fluorescence, Phys. Rev. Lett. 96 (11) (2006) 113002.

[43] S. Kühn, et al., Enhancement of single-molecule fluorescence using a gold nanoparticle as an optical nanoantenna, Phys. Rev. Lett. 97 (1) (2006) 017402.

[44] A. Kinkhabwala, et al., Large single-molecule fluorescence enhancements produced by a bowtie nanoantenna, Nat. Photon. 3 (11) (2009) 654–657.

[45] G.M. Akselrod, et al., Probing the mechanisms of large Purcell enhancement in plasmonic nanoantennas, Nat. Photon. 8 (11) (2014) 835–840.

[46] I.L. Medintz, et al., Quantum dot bioconjugates for imaging, labelling and sensing, Nat. Mater. 4 (6) (2005) 435–446.

[47] J.F.-C. Loo, et al., Upconversion and downconversion nanoparticles for biophotonics and nanomedicine, Coord. Chem. Rev. 400 (2019) 213042.

[48] M.L. Bhaumik, C.L. Telk, Fluorescence quantum efficiency of rare-earth chelates, J. Opt. Soc. Am. 54 (10) (1964) 1211–1214.

[49] Y. Kim, et al., Recent advances in quantum nanophotonics: plexcitonic and vibro-polaritonic strong coupling and its biomedical and chemical applications, Nanophotonics 12 (3) (2023) 413–439.

[50] M. Toma, et al., Surface plasmon-coupled emission on plasmonic Bragg gratings, Opt. Express 20 (13) (2012) 14042.

[51] K. Sergelen, et al., Plasmon field-enhanced fluorescence energy transfer for hairpin aptamer assay readout, ACS Sens. 2 (7) (2017) 916–923.

[52] J. Wenger, et al., Emission and excitation contributions to enhanced single molecule fluorescence by gold nanometric apertures, Opt. Express 16 (5) (2008) 3008.

[53] W.L. Barnes, Fluorescence near interfaces: the role of photonic mode density, J. Mod. Opt. 45 (4) (1998) 661–699.

[54] K. Vasilev, W. Knoll, M. Kreiter, Fluorescence intensities of chromophores in front of a thin metal film, J. Chem. Phys. 120 (7) (2004) 3439–3445.

[55] M. Bauch, S. Hageneder, J. Dostalek, Plasmonic amplification for bioassays with epi-fluorescence readout, Opt. Express 22 (26) (2014) 32026.

[56] Y. Wang, et al., Directional fluorescence emission co-enhanced by localized and propagating surface plasmons for biosensing, Nanoscale 8 (15) (2016) 8008–8016.

[57] M. Bauch, J. Dostalek, Collective localized surface plasmons for high performance fluorescence biosensing, Opt. Express 21 (17) (2013) 20470.

[58] A. Devilez, B. Stout, N. Bonod, Compact metallo-dielectric optical antenna for ultra directional and enhanced radiative emission, ACS Nano 4 (6) (2010) 3390–3396.

[59] F. Zhu, et al., Optical ultracompact directional antennas based on a dimer nanorod structure, Nanomater. 12 (16) (2022) 2841.

[60] T. Coenen, et al., Directional emission from plasmonic yagi–uda antennas probed by angle-resolved cathodoluminescence spectroscopy, Nano Lett. 11 (9) (2011) 3779–3784.

[61] D.F. Cruz, et al., Ultrabright fluorescence readout of an inkjet-printed immunoassay using plasmonic nanogap cavities, Nano Lett. 20 (6) (2020) 4330–4336.

[62] D. Axelrod, a.T.P. Burghardt, N.L. Thompson, Total internal reflection fluorescence, Annu. Rev. Biophys. Bioeng. 13 (1) (1984) 247–268.

[63] D. Geilfuss, et al., Can classical surface plasmon resonance advance via the coupling to other analytical approaches? Front. Anal. Sci. 2 (2022).

[64] B. Lechner, et al., In situ monitoring of rolling circle amplification on a solid support by surface plasmon resonance and optical waveguide spectroscopy, ACS Appl. Mater. & Interfac. 13 (27) (2021) 32352–32362.

[65] T. Riedel, et al., Plasmonic hepatitis B biosensor for the analysis of clinical saliva, Anal. Chem. 89 (5) (2017) 2972–2977.

[66] J. Luan, et al., Add-on plasmonic patch as a universal fluorescence enhancer, Light Sci. Appl. 7 (1) (2018) 29.

[67] C. Vietz, et al., Benchmarking smartphone fluorescence-based microscopy with DNA origami nanobeads: reducing the gap toward single-molecule sensitivity, ACS Omega 4 (1) (2019) 637–642.

[68] K. Trofymchuk, et al., Addressable nanoantennas with cleared hotspots for single-molecule detection on a portable smartphone microscope, Nat. Commun. 12 (1) (2021).

[69] W.-I. Lee, et al., A smartphone imaging-based label-free and dual-wavelength fluorescent biosensor with high sensitivity and accuracy, Biosens. Bioelectron. 94 (2017) 643–650.

[70] D. Punj, et al., Self-assembled nanoparticle dimer antennas for plasmonic-enhanced single-molecule fluorescence detection at micromolar concentrations, ACS Photon. 2 (8) (2015) 1099–1107.

[71] X. Lu, D. Punj, M. Orrit, Two-photon-excited single-molecule fluorescence enhanced by gold nanorod dimers, Nano Lett. 22 (10) (2022) 4215–4222.

[72] W. Zhang, et al., Plasmonic enhancement of two-photon-excited luminescence of single quantum dots by individual gold nanorods, ACS Photon. 5 (7) (2018) 2960–2968.

[73] G.P. Acuna, et al., Fluorescence enhancement at docking sites of DNA-directed self-assembled nanoantennas, Sci. 338 (6106) (2012) 506–510.

[74] K. Trofymchuk, et al., Gold nanorod DNA origami antennas for 3 orders of magnitude fluorescence enhancement in NIR, ACS Nano 17 (2) (2023) 1327–1334.

[75] C. Vietz, et al., Broadband fluorescence enhancement with self-assembled silver nanoparticle optical antennas, ACS Nano 11 (5) (2017) 4969–4975.

[76] A. Minopoli, et al., Ultrasensitive antibody-aptamer plasmonic biosensor for malaria biomarker detection in whole blood, Nat. Commun. 11 (1) (2020) 6134.

[77] A. Minopoli, et al., Double-resonant nanostructured gold surface for multiplexed detection, ACS Appl. Mater. & Interfac. 14 (5) (2022) 6417–6427.

[78] J.S. Pang, et al., Tunable three-dimensional plasmonic arrays for large near-infrared fluorescence enhancement, ACS Appl. Mater. & Interfac. 11 (26) (2019) 23083–23092.

[79] K. Schmidt, et al., Rolling circle amplification tailored for plasmonic biosensors: from ensemble to single-molecule detection, ACS Appl. Mater. & Interfac. 14 (49) (2022) 55017–55027.

[80] A. Bozdogan, et al., Development of a specific troponin I detection system with enhanced immune sensitivity using a single monoclonal antibody, R. Soc. Open Sci. 7 (10) (2020) 200871.

[81] D. Etezadi, et al., Nanoplasmonic mid-infrared biosensor for in vitro protein secondary structure detection, Light Sci. Appl. 6 (8) (2017) e17029.

[82] S. Hageneder, et al., Responsive hydrogel binding matrix for dual signal amplification in fluorescence affinity biosensors and peptide microarrays, ACS Appl. Mater. & Interfac. 13 (23) (2021) 27645–27655.

[83] M. Oliverio, et al., Chemical functionalization of plasmonic surface biosensors: a tutorial review on issues, strategies, and costs, ACS Appl. Mater. & Interfac. 9 (35) (2017) 29394–29411.

[84] N.G. Quilis, et al., UV-laser interference lithography for local functionalization of plasmonic nanostructures with responsive hydrogel, J. Phys. Chem. C 124 (5) (2020) 3297–3305.

[85] J. Svirelis, et al., Stable trapping of multiple proteins at physiological conditions using nanoscale chambers with macromolecular gates, Nat. Commun. 14 (1) (2023).

[86] N. Zhang, et al., High sensitivity molecule detection by plasmonic nanoantennas with selective binding at electromagnetic hotspots, Nanoscale 6 (3) (2014) 1416–1422.

[87] S. Simoncelli, et al., Nanoscale control of molecular self-assembly induced by plasmonic hot-electron dynamics, ACS Nano 12 (3) (2018) 2184–2192.

[88] Y. Wang, et al., Plasmon-directed polymerization: regulating polymer growth with light, Nano Res. 11 (12) (2018) 6384–6390.

[89] H. Chen, et al., Gold nanorods and their plasmonic properties, Chem. Soc. Rev. 42 (7) (2013) 2679–2724.

[90] V. Glembockyte, et al., DNA origami nanoantennas for fluorescence enhancement, Acc. Chem. Res. 54 (17) (2021) 3338–3348.

[91] Y.-S. Wang, et al., Functional biointerfaces based on mixed zwitterionic self-assembled monolayers for biosensing applications, Langmuir 35 (5) (2019) 1652–1661.

[92] Q. Li, et al., Zwitterionic biomaterials, Chem. Rev. 122 (23) (2022) 17073–17154.

[93] H. Vaisocherová, et al., Functionalized ultra-low fouling carboxy- and hydroxy-functional surface platforms: functionalization capacity, biorecognition capability and resistance to fouling from undiluted biological media, Biosens. Bioelectron. 51 (2014) 150–157.

[94] F. Diehl, et al., Plasmonic nanomaterials with responsive polymer hydrogels for sensing and actuation, Chem. Soc. Rev. 51 (10) (2022) 3926–3963.

[95] C.J. Huang, J. Dostalek, W. Knoll, Long range surface plasmon and hydrogel optical waveguide field-enhanced fluorescence biosensor with 3D hydrogel binding matrix: on the role of diffusion mass transfer, Biosens. Bioelectron. 26 (4) (2010) 1425–1431.

[96] J.-H. Lee, et al., Nondestructive characterization of stem cell neurogenesis by a magneto-plasmonic nanomaterial-based exosomal miRNA detection, ACS Nano 13 (8) (2019) 8793–8803.

[97] G.M. Santos, et al., Label-free, zeptomole cancer biomarker detection by surface-enhanced fluorescence on nanoporous gold disk plasmonic nanoparticles, J. Biophot. 8 (10) (2015) 855–863.

[98] A.T. Reiner, S. Fossati, J. Dostalek, Biosensor platform for parallel surface plasmon-enhanced epifluorescence and surface plasmon resonance detection, Sens. Actuator. B Chem. 257 (2018) 594–601.

[99] F. Zang, et al., Ultrasensitive Ebola virus antigen sensing via 3D nanoantenna arrays, Adv. Mater. 31 (30) (2019) 1902331.

[100] N. Ullah Khan, et al., Ultrasensitive detection of exosome using biofunctionalized gold nanorods on a silver-island film, Nano Lett. 21 (13) (2021) 5532–5539.

[101] Z.A.R. Jawad, et al., Highly sensitive plasmonic detection of the pancreatic cancer biomarker CA 19-9, Sci. Rep. 7 (1) (2017) 14309.

[102] X. Li, et al., Multiplexed anti-toxoplasma IgG, IgM, and IgA assay on plasmonic gold chips: towards making mass screening possible with dye test precision, J. Clin. Microbiol. 54 (7) (2016) 1726–1733.

[103] E. Chou, et al., A fluorescent plasmonic biochip assay for multiplex screening of diagnostic serum antibody targets in human Lyme disease, PLoS One 15 (2) (2020).

[104] J. Luan, et al., Ultrabright fluorescent nanoscale labels for the femtomolar detection of analytes with standard bioassays, Nat. Biomed. Eng. 4 (5) (2020) 518–530.

[105] B. Zhang, et al., A plasmonic chip for biomarker discovery and diagnosis of type 1 diabetes, Nat. Med. 20 (8) (2014) 948–953.

[106] Y. Pang, et al., A fluorescent aptasensor for H5N1 influenza virus detection based-on the core–shell nanoparticles metal-enhanced fluorescence (MEF), Biosens. Bioelectron. 66 (2015) 527–532.

[107] N. Sui, et al., Selective and sensitive biosensors based on metal-enhanced fluorescence, Sens. Actuator. B Chem. 202 (2014) 1148–1153.

[108] W. Palau, et al., Direct evidence for RNA–RNA interactions at the 3′ end of the Hepatitis C virus genome using surface plasmon resonance, RNA 19 (7) (2013) 982–991.

[109] K. Schmidt, et al., Sandwich immuno-RCA assay with single molecule counting readout: the importance of biointerface design, Acs Appl. Mater. & Interfac. 16 (14) (2024) 17109–17119.

[110] G. Qiu, et al., Thermoplasmonic-assisted cyclic cleavage amplification for self-validating plasmonic detection of SARS-CoV-2, ACS Nano 15 (4) (2021) 7536–7546.

[111] Y. Wu, et al., Recent advances in catalytic hairpin assembly signal amplification-based sensing strategies for microRNA detection, Talanta 235 (2021) 122735.

[112] K. Shi, N. Na, J. Ouyang, Label- and enzyme-free plasmon-enhanced single molecule fluorescence detection of HIV DNA fragments based on a catalytic hairpin assembly, Analyst 147 (4) (2022) 604–613.

[113] J. Liu, et al., Applications of catalytic hairpin assembly reaction in biosensing, Small 15 (42) (2019) 1902989.

[114] Y. Zhou, et al., An ultrasensitive fluorescence detection template of pathogenic bacteria based on dual catalytic hairpin DNA Walker@Gold nanoparticles enzyme-free amplification, Spectrochim. Acta Mol. Biomol. Spectrosc. 277 (2022) 121259.

[115] G.-X. Liang, et al., A potent fluorescent biosensor integrating 3D DNA walker with localized catalytic hairpin assembly for highly sensitive and enzyme-free Zika virus detection, Sens. Actuator. B Chem. 354 (2022) 131199.

[116] T. Zhao, et al., Optically programmable plasmon enhanced fluorescence-catalytic hairpin assembly signal amplification strategy for spatiotemporally precise imaging, Anal. Chem. 94 (13) (2022) 5399–5405.

[117] J. Ferlay, et al., Cancer statistics for the year 2020: an overview, Int. J. Cancer 149 (2021) 778–789.

[118] D. Sabry, et al., Role of miRNA-210, miRNA-21 and miRNA-126 as diagnostic biomarkers in colorectal carcinoma: impact of HIF-1α-VEGF signaling pathway, Mol. Cell. Biochem. 454 (1) (2019) 177–189.

[119] H. Wang, et al., microRNA-21 promotes breast cancer proliferation and metastasis by targeting LZTFL1, BMC Cancer 19 (1) (2019) 738.

[120] B. Shao, et al., Plasma microRNAs predict chemoresistance in patients with metastatic breast cancer, Technol. Cancer Res. Treat. 18 (2019) 1533033819828709.

[121] L. Liang, et al., Metal-enhanced fluorescence/visual bimodal platform for multiplexed ultrasensitive detection of microRNA with reusable paper analytical devices, Biosens. Bioelectron. 95 (2017) 181–188.

[122] M. Peng, et al., Target-triggered assembly of nanogap antennas to enhance the fluorescence of single molecules and their application in MicroRNA detection, Small 16 (19) (2020) 2000460.

[123] T. Wei, et al., Rapid and sensitive detection of microRNA via the capture of fluorescent dyes-loaded albumin nanoparticles around functionalized magnetic beads, Biosens. Bioelectron. 94 (2017) 56–62.

[124] P. Jia, et al., DNA precisely regulated Au nanorods/Ag2S quantum dots satellite structure for ultrasensitive detection of prostate cancer biomarker, Sens. Actuator. B Chem. 347 (2021) 130585.

[125] J.-H. Choi, et al., CRISPR-Cas12a-Based nucleic acid amplification-free DNA biosensor via Au nanoparticle-assisted metal-enhanced fluorescence and colorimetric analysis, Nano Lett. 21 (1) (2021) 693–699.

[126] G. Sahoo, et al., A review on caspases: key regulators of biological activities and apoptosis, Mol. Neurobiol. 60 (10) (2023) 5805–5837.

[127] J.H. Choi, J.W. Choi, Metal-enhanced fluorescence by bifunctional Au nanoparticles for highly sensitive and simple detection of proteolytic enzyme, Nano Lett. 20 (10) (2020) 7100–7107.

[128] R. Gupta, et al., Ultrasensitive lateral-flow assays via plasmonically active antibody-conjugated fluorescent nanoparticles, Nat. Biomed. Eng. 7 (12) (2023) 1556–1570.

[129] J. Liu, et al., An ultra-sensitive and specific nanoplasmonic-enhanced isothermal amplification platform for the ultrafast point-of-care testing of SARS-CoV-2, Chem. Eng. J. 451 (2023) 138822.

[130] A. Minopoli, et al., Ultrasensitive antibody-aptamer plasmonic biosensor for malaria biomarker detection in whole blood, Nat. Commun. 11 (1) (2020) 6134.

[131] J.P. Dubey, J.L. Jones, Toxoplasma gondii infection in humans and animals in the United States, Int. J. Parasitol. 38 (11) (2008) 1257–1278.

[132] K. Shi, N. Na, J. Ouyang, Label- and enzyme-free plasmon-enhanced single molecule fluorescence detection of HIV DNA fragments based on a catalytic hairpin assembly, Analyst 147 (4) (2022) 604–613.

[133] M. Maltz-Matyschsyk, et al., Development of a biomarker signature using grating-coupled fluorescence plasmonic microarray for diagnosis of MIS-C, Front. Bioeng. Biotechnol. 11 (2023).

[134] X. Li, et al., Multiplexed anti-toxoplasma IgG, IgM, and IgA assay on plasmonic gold chips: towards making mass screening possible with dye test precision, J. Clin. Microbiol. 54 (7) (2016) 1726–1733.

[135] A. Mensah George, A. Roth Gregory, V. Fuster, The global burden of cardiovascular diseases and risk factors, J. Am. Coll. Cardiol. 74 (20) (2019) 2529–2532.

[136] K. Toma, et al., Surface plasmon-enhanced fluorescence immunosensor for monitoring cardiac troponin I, Sensor. Actuator. B Chem. 368 (2022) 132132.

[137] P. Zheng, et al., Plasmon-enhanced near-infrared fluorescence detection of traumatic brain injury biomarker glial fibrillary acidic protein in blood plasma, Anal. Chim. Acta 1203 (2022) 339721.

[138] J.-H. Hwang, et al., DNA-engineerable ultraflat-faceted core–shell nanocuboids with strong, quantitative plasmon-enhanced fluorescence signals for sensitive, reliable MicroRNA detection, Nano Lett. 21 (5) (2021) 2132–2140.

[139] G. Morris, C.R. Reschke, D.C. Henshall, Targeting microRNA-134 for seizure control and disease modification in epilepsy, EBioMed. 45 (2019) 646–654.

[140] H.-p. Zhang, et al., Circulating microRNA 134 sheds light on the diagnosis of major depressive disorder, Transl. Psychiatr. 10 (1) (2020) 95.

[141] Y. Ye, et al., Role of MicroRNA in governing synaptic plasticity, Neural Plast. 2016 (2016) 4959523.

[142] Y. Cui, et al., Core–shell gold nanocubes for point mutation detection based on plasmon-enhanced fluorescence, J. Mater. Chem. B 5 (27) (2017) 5329–5335.

[143] C. Niu, et al., Near-infrared-fluorescent probes for bioapplications based on silica-coated gold nanobipyramids with distance-dependent plasmon-enhanced fluorescence, Anal. Chem. 88 (22) (2016) 11062–11069.

[144] K. Eyer, et al., Single-cell deep phenotyping of IgG-secreting cells for high-resolution immune monitoring, Nat. Biotechnol. 35 (10) (2017) 977–982.

[145] M.C. Tanzer, et al., Quantitative and dynamic catalogs of proteins released during apoptotic and necroptotic cell death, Cell Rep. 30 (4) (2020) 1260–1270.e5.

[146] M. Huse, E.J. Quann, M.M. Davis, Shouts, whispers and the kiss of death: directional secretion in T cells, Nat. Immunol. 9 (10) (2008) 1105–1111.

[147] C. Ma, et al., A clinical microchip for evaluation of single immune cells reveals high functional heterogeneity in phenotypically similar T cells, Nat. Med. 17 (6) (2011) 738–743.

[148] Y. Lu, et al., Highly multiplexed profiling of single-cell effector functions reveals deep functional heterogeneity in response to pathogenic ligands, Proc. Natl. Acad. Sci. U.S.A. 112 (7) (2015) E607–E615.

[149] J.W. Hellinger, et al., Identification of drivers of breast cancer invasion by secretome analysis: insight into CTGF signaling, Sci. Rep. 10 (1) (2020) 17889.

[150] N. Joubert, et al., Antibody–drug conjugates: the last decade, Pharmaceut. 13 (9) (2020) 245.

[151] Y. Gao, et al., More symmetrical "hot spots" ensure stronger plasmon-enhanced fluorescence: from Au nanorods to nanostars, Anal. Chem. 93 (4) (2021) 2480–2489.

[152] S. Xu, et al., Gold nanobipyramids as dual-functional substrates for in situ "turn on" analyzing intracellular telomerase activity based on target-triggered plasmon-enhanced fluorescence, ACS Appl. Mater. & Interfac. 10 (32) (2018) 26851–26858.

[153] D. Li, et al., Spatiotemporally controlled ultrasensitive molecular imaging using a DNA computation-mediated DNAzyme platform, Anal. Chem. 94 (41) (2022) 14467–14474.

[154] J. Chen, et al., DNA computation-modulated self-assembly of stimuli-responsive plasmonic nanogap antennas for correlated multiplexed molecular imaging, Anal. Chem. 94 (48) (2022) 16887–16893.

[155] T. Zhao, et al., Fluorescence-enhanced dual-driven "OR-AND" DNA logic platform for accurate cell subtype identification, Anal. Chem. 95 (6) (2023) 3525–3531.

[156] H. Xiao, et al., A gold-nanodot-decorated hollow carbon nanosphere based nanoplatform for intracellular miRNA imaging in colorectal cancer cells, Chem. Commun. 55 (82) (2019) 12352–12355.

[157] K. Tawa, et al., In situ sensitive fluorescence imaging of neurons cultured on a plasmonic dish using fluorescence microscopy, ACS Appl. Mater. Interfac. 6 (22) (2014) 20010–20015.

[158] K. Tawa, et al., Fluorescence microscopy imaging of cells with a plasmonic dish integrally molded, Jpn. J. Appl. Phys. 55 (3S2) (2016) 03DF12.

[159] S. Masuda, et al., High-resolution imaging of a cell-attached nanointerface using a gold-nanoparticle two-dimensional sheet, Sci. Rep. 7 (1) (2017) 3720.

[160] I.G. Theodorou, et al., Towards multiplexed near-infrared cellular imaging using gold nanostar arrays with tunable fluorescence enhancement, Nanoscale 11 (4) (2019) 2079–2088.

[161] A. Seth, et al., High-resolution imaging of protein secretion at the single-cell level using plasmon-enhanced FluoroDOT assay, Cell Rep. Methods 2 (8) (2022) 100267.

[162] M.S. Braga, et al., Portable multispectral colorimeter for metallic ion detection and classification, Sens 17 (8) (2017) 1730.

[163] H.N. Ekramul Mahmud, A.K.O. Huq, R.b. Yahya, ChemInform abstract: the removal of heavy metal ions from wastewater/aqueous solution using polypyrrole-based adsorbents: a review, ChemInform 47 (13) (2016).

[164] H. Zhang, et al., Polyacrylonitrile/noble metal/SiO2 nanofibers as substrates for the amplified detection of picomolar amounts of metal ions through plasmon-enhanced fluorescence, Nanoscale 7 (4) (2015) 1374–1382.

[165] L. Zhou, et al., Amplified detection of iron ion based on plasmon enhanced fluorescence and subsequently fluorescence quenching, Nano-Micro Lett. 6 (4) (2014) 327–334.

[166] K. Dong, et al., Sensitive Hg2+ ion detection using metal enhanced fluorescence of novel polyvinyl pyrrolidone (PVP)-Templated gold nanoparticles, Appl. Spectrosc. 72 (11) (2018) 1645–1652.

[167] G. Lin, W. Dong, R. Zhang, Plasmon enhanced fluorescence of photosynthetic complexes by conjugating with gold micro-plates and their single-particle sensing application, Sens. Actuator. B Chem. 371 (2022) 132525.

[168] X. Niu, et al., A "turn-on" fluorescence sensor for Pb2+ detection based on graphene quantum dots and gold nanoparticles, Sens. Actuator. B Chem. 255 (2018) 1577–1581.

[169] B. Sun, et al., Metal-enhanced fluorescence-based multilayer core–shell Ag-nanocube@SiO2@PMOs nanocomposite sensor for Cu2+ detection, RSC Adv. 6 (66) (2016) 61109–61118.

[170] J.K. Kim, D.-J. Jang, Metal-enhanced fluorescence of gold nanoclusters adsorbed onto Ag@SiO2 core–shell nanoparticles, J. Mater. Chem. C 5 (24) (2017) 6037–6046.

[171] X.-P. Zhang, et al., Single gold nanocluster probe-based fluorescent sensor array for heavy metal ion discrimination, J. Hazard Mater. 405 (2021) 124259.

[172] N. Kaewnok, et al., Silver nanoparticle incorporated colorimetric/fluorescence sensor for sub-ppb detection of mercury via plasmon-enhanced fluorescence strategy, J. Photochem. Photobiol. Chem. 433 (2022) 114140.

[173] S. Wang, et al., Carbon dot- and gold nanocluster-based three-channel fluorescence array sensor: visual detection of multiple metal ions in complex samples, Sensor. Actuator. B Chem. 369 (2022) 132194.

[174] J.F. Olorunyomi, et al., Fabrication of a reusable carbon dot/gold nanoparticle/metal–organic framework film for fluorescence detection of lead ions in water, ACS Appl. Mater. & Interfac. 14 (31) (2022) 35755–35768.

[175] Y. Pang, et al., "Turn on" and label-free core−shell Ag@SiO2 nanoparticles-based metal-enhanced fluorescent (MEF) aptasensor for Hg2+, Sci. Rep. 5 (1) (2015) 9451.

[176] J.-H. Lin, et al., The detection of Mercury(II) ions using fluorescent gold nanoclusters on a portable paper-based device, Chem. Eng. J. 430 (2022) 133070.

[177] S. Bothra, et al., Chemically modified cellulose strips with pyridoxal conjugated red fluorescent gold nanoclusters for nanomolar detection of mercuric ions, Biosens. Bioelectron. 90 (2017) 329–335.

[178] Z. Cheng, G. Li, M. Liu, Metal-enhanced fluorescence effect of Ag and Au nanoparticles modified with rhodamine derivative in detecting Hg2+, Sens. Actuator. B Chem. 212 (2015) 495–504.

[179] H. Li, et al., AuNS@Ag core-shell nanocubes grafted with rhodamine for concurrent metal-enhanced fluorescence and surfaced enhanced Raman determination of mercury ions, Anal. Chim. Acta 1018 (2018) 94–103.

[180] Z. Cheng, G. Li, M. Liu, A metal-enhanced fluorescence sensing platform based on new mercapto rhodamine derivatives for reversible Hg2+ detection, J. Hazard Mater. 287 (2015) 402–411.

[181] H. Zhuang, et al., A novel polypeptide-modified fluorescent gold nanoclusters for copper ion detection, Sci. Rep. 12 (1) (2022) 6624.

[182] J. Xu, et al., Copper nanoclusters-based fluorescent sensor array to identify metal ions and dissolved organic matter, J. Hazard Mater. 428 (2022) 128158.

[183] I. El-Nahhal, Y. El-Nahhal, Pesticide residues in drinking water, their potential risk to human health and removal options, J. Environ. Manag. (2021) 299.

[184] O. Golge, F. Hepsag, B. Kabak, Health risk assessment of selected pesticide residues in green pepper and cucumber, Food Chem. Toxicol. 121 (2018) 51–64.

[185] Y. Mehmood, et al., Pesticide residues, health risks, and vegetable farmers' risk perceptions in Punjab, Pakistan, Human Ecol. Risk Assess. 27 (3) (2021) 846–864.

[186] Y.C. Chou, et al., High-efficient screening of pesticide residues in vegetables using gas chromatography/quadrupole time-of-flight (GC/Q-TOF), J. Food Compos. Anal. 126 (2024).

[187] A. Zandi, M. Amjadi, T. Hallaj, Plasmon-enhanced fluorimetric and colorimetric dual sensor based on fluorescein/Ag nanoprisms for sensitive determination of mancozeb, Food Chem. (2022) 369.

[188] Q. Luo, et al., An ultrasensitive fluorescent sensor for organophosphorus pesticides detection based on RB-Ag/Au bimetallic nanoparticles, Sens. Actuator. B Chem. 263 (2018) 517–523.

[189] Y. Cai, et al., Capsulation of AuNCs with AIE effect into metal–organic framework for the marriage of a fluorescence and colorimetric biosensor to detect organophosphorus pesticides, Anal. Chem. 93 (19) (2021) 7275–7282.

[190] D. Wei, et al., Encapsulating gold nanoclusters into metal–organic frameworks to boost luminescence for sensitive detection of copper ions and organophosphorus pesticides, J. Hazard Mater. 441 (2023) 129890.

[191] T. Jin, et al., Ag@SiO2 nanoparticles performing as a nanoprobe for selective analysis of 2-aminoanthracene in wastewater samples via metal-enhanced fluorescence, Talanta 200 (2019) 242–248.

[192] H.-X. Ren, et al., A fluorescent detection for paraquat based on β-CDs-enhanced fluorescent gold nanoclusters, Foods 10 (6) (2021) 1178.

[193] L. Su, et al., Fluorescent aptasensor for carbendazim detection in aqueous samples based on gold nanoparticles quenching Rhodamine B, Spectrochim. Acta Mol. Biomol. Spectrosc. 225 (2020) 117511.

[194] Y. Jin, et al., In situ reduction triggers the highly sensitive detection of pesticide by classic gold nanoparticle and quantum dots nanocomposite, Anal. Chim. Acta 1172 (2021) 338679.

[195] K. Wang, et al., A fluorescence and localized surface plasmon resonance dual-readout sensing strategy for detection of acetamiprid and organophosphorus pesticides, Sens. Actuator. B Chem. 351 (2022) 130977.

[196] X.-L. Yin, et al., Multicolor enzyme-linked immunosorbent sensor for sensitive detection of organophosphorus pesticides based on TMB2+-mediated etching of gold nanorods, Microchem. J. 168 (2021) 106411.

[197] S.K. Tuteja, et al., Synthesis and characterization of silica-coated silver nanoprobe for paraoxon pesticide detection, BioNanoSci. 4 (2) (2014) 149–156.

[198] M.S. Kim, G.W. Kim, T.J. Park, A facile and sensitive detection of organophosphorus chemicals by rapid aggregation of gold nanoparticles using organic compounds, Biosens. Bioelectron. 67 (2015) 408–412.

[199] N.M. Dissanayake, et al., Highly sensitive plasmonic metal nanoparticle-based sensors for the detection of organophosphorus pesticides, Talanta 200 (2019) 218–227.

[200] S.-H. Hung, et al., Gold-nanoparticle-based fluorescent "turn-on" sensor for selective and sensitive detection of dimethoate, Food Chem. 260 (2018) 61–65.

[201] G. Chen, et al., A sensitive bio-barcode immunoassay based on bimetallic Au@Pt nanozyme for detection of organophosphate pesticides in various agro-products, Food Chem. 362 (2021) 130118.

[202] H. Yu, et al., Dual-mode detection of organophosphate pesticides in pear and Chinese cabbage based on fluorescence and AuNPs colorimetric assays, Food Chem. 364 (2021) 130326.

[203] P. Alfonso-Muniozguren, et al., A review on pharmaceuticals removal from waters by single and combined biological, membrane filtration and ultrasound systems, Ultrason. Sonochem. 76 (2021).

[204] S.D. Kayode-Afolayan, E.F. Ahuekwe, O.C. Nwinyi, Impacts of pharmaceutical effluents on aquatic ecosystems, Sci. Afr. 17 (2022).

[205] Y.J. Ben, et al., Human health risk assessment of antibiotic resistance associated with antibiotic residues in the environment: a review, Environ. Res. 169 (2019) 483–493.

[206] A. Moaddab, S. Ghasemi, Green synthesis of silver/carbon dot nanoparticles from Malva Sylvestris for fluorescence determination of tetracycline, Microchem. J. (2021) 166.

[207] J. Xu, et al., Metal-enhanced fluorescence detection and degradation of tetracycline by silver nanoparticle-encapsulated halloysite nano-lumen, J. Hazard Mater. (2020) 386.

[208] R. Jalili, et al., A ratiometric fluorescent probe based on carbon dots and gold nanocluster encapsulated metal–organic framework for detection of cephalexin residues in milk, Spectrochim. Acta Mol. Biomol. Spectrosc. 262 (2021) 120089.

[209] S.-N. Yin, et al., Novel metal nanoparticle-enhanced fluorescence for determination of trace amounts of fluoroquinolone in aqueous solutions, Talanta 174 (2017) 14–20.

[210] B. Fu, et al., A highly stable, rapid and sensitive fluorescent probe for ciprofloxacin based on Al3+-enhanced fluorescence of gold nanoclusters, Sens. Actuator. B Chem. 346 (2021) 130502.

[211] M. Amjadi, L. Farzampour, Fluorescence quenching of fluoroquinolones by gold nanoparticles with different sizes and its analytical application, J. Lumin. 145 (2014) 263–268.

[212] Y. Geng, et al., Aptamer act as fluorescence switching of bovine serum albumin stabilized gold nanoclusters for ultrasensitive detection of kanamycin in milk, Microchem. J. 165 (2021) 106145.

[213] M. Ramezani, et al., A selective and sensitive fluorescent aptasensor for detection of kanamycin based on catalytic recycling activity of exonuclease III and gold nanoparticles, Sens. Actuator. B Chem. 222 (2016) 1–7.

[214] J. Larkin, et al., Length-independent DNA packing into nanopore zero-mode waveguides for low-input DNA sequencing, Nat. Nanotechnol. 12 (12) (2017) 1169–1175.

[215] M. Baibakov, et al., Zero-mode waveguides can be made better: fluorescence enhancement with rectangular aluminum nanoapertures from the visible to the deep ultraviolet, Nanoscale Adv. 2 (9) (2020) 4153–4160.

[216] O.N. Assad, et al., Light-enhancing plasmonic-nanopore biosensor for superior single-molecule detection, Adv. Mater. 29 (9) (2017) 1605442.

[217] C. Chen, et al., High spatial resolution nanoslit SERS for single-molecule nucleobase sensing, Nat. Commun. 9 (1) (2018) 1733.

[218] D. Garoli, et al., Plasmonic nanopores for single-molecule detection and manipulation: toward sequencing applications, Nano Lett. 19 (11) (2019) 7553–7562.

[219] D. Punj, et al., A plasmonic 'antenna-in-box' platform for enhanced single-molecule analysis at micromolar concentrations, Nat. Nanotechnol. 8 (7) (2013) 512–516.

[220] J. Chen, et al., High-throughput platform for real-time monitoring of biological processes by multicolor single-molecule fluorescence, Proc. Natl. Acad. Sci. USA 111 (2) (2014) 664–669.

[221] S. Khatua, H. Yuan, M. Orrit, Enhanced-fluorescence correlation spectroscopy at micro-molar dye concentration around a single gold nanorod, Phys. Chem. Chem. Phys. 17 (33) (2015) 21127–21132.

[222] M. Dass, et al., DNA origami-enabled plasmonic sensing, J. Phys. Chem. C 125 (11) (2021) 5969–5981.

[223] T. Zhang, et al., Single-particle spectroscopic study on fluorescence enhancement by plasmon coupled gold nanorod dimers assembled on DNA origami, J. Phys. Chem. Lett. 6 (11) (2015) 2043–2049.

[224] L. Grabenhorst, et al., Fluorophore photostability and saturation in the hotspot of DNA origami nanoantennas, Methods Appl. Fluoresc. 8 (2) (2020) 024003.

[225] S. Tiwari, et al., Achieving high temporal resolution in single-molecule fluorescence techniques using plasmonic nanoantennas, Adv. Opt. Mater. 11 (13) (2023) 2300168.

[226] S.E. Ochmann, et al., Optical nanoantenna for single molecule-based detection of Zika virus nucleic acids without molecular multiplication, Anal. Chem. 89 (23) (2017) 13000–13007.

[227] M. Pfeiffer, et al., Single antibody detection in a DNA origami nanoantenna, iSci. 24 (9) (2021) 103072.

[228] X. Wang, L. Zhang, A. Hao, Z. Shi, C. Dai, Y. Yang, et al., Silica-coated silver nanoparticles decorated with fluorescent CdTe quantum dots and DNA aptamers for detection of tetracycline, ACS Appl. Nano Mater. 3 (2020) 9796–9803, https://doi.org/10.1021/acsanm.0c01890.